

On the biogenicity of Fe-oxyhydroxide filaments in silicified low-temperature hydrothermal deposits: Implications for the identification of Fe-oxidizing bacteria in the rock record

Karen C. Johannessen¹  | Nicola McLoughlin²  | Per Erik Vullum^{3,4} |
Ingunn H. Thorseth¹

¹K. G. Jebsen Centre for Deep Sea Research and Department of Earth Science, University of Bergen, Bergen, Norway

²Department of Geology and the Albany Museum, Rhodes University, Grahamstown, South Africa

³Department of Materials and Nanotechnology, SINTEF Industry, Trondheim, Norway

⁴Department of Physics, Norwegian University of Science and Technology (NTNU), Trondheim, Norway

Correspondence

Karen C. Johannessen, K. G. Jebsen Centre for Deep Sea Research and Department of Earth Science, University of Bergen, Allégaten 41, 5007 Bergen, Norway.
Email: Karen.C.Johannessen@uib.no

Funding information

University of Bergen and the Research Council of Norway through the Centre for Geobiology, Grant/Award Number: 179560; Foundation Kristian Gerhard Jebsen; Bergen Research Foundation; NTNU NanoLab through the Norwegian Micro- and Nano-Fabrication Facility, NorFab, Grant/Award Number: 197411/V30; NORTEM infrastructure, Grant/Award Number: 197405; TEM Gemini Centre; DST-NRF Centre for Excellence in Palaeosciences at the University of Witwatersrand

Abstract

Microaerophilic Fe(II)-oxidizing bacteria produce biomineralized twisted and branched stalks, which are promising biosignatures of microbial Fe oxidation in ancient jaspers and iron formations. Extracellular Fe stalks retain their morphological characteristics under experimentally elevated temperatures, but the extent to which natural post-depositional processes affect fossil integrity remains to be resolved. We examined siliceous Fe deposits from laminated mounds and chimney structures from an extinct part of the Jan Mayen Vent Fields on the Arctic Mid-Ocean Ridge. Our aims were to determine how early seafloor diagenesis affects morphological and chemical signatures of Fe-oxyhydroxide biomineralization and how extracellular stalks differ from abiogenic features. Optical and scanning electron microscopy in combination with focused ion beam-transmission electron microscopy (FIB-TEM) was used to study the filamentous textures and cross sections of individual stalks. Our results revealed directional, dendritic, and radial arrangements of biogenic twisted stalks and randomly organized networks of hollow tubes. Stalks were encrusted by concentric Fe-oxyhydroxide laminae and silica casings. Element maps produced by energy dispersive X-ray spectroscopy (EDS) in TEM showed variations in the content of Si, P, and S within filaments, demonstrating that successive hydrothermal fluid pulses mediate early diagenetic alteration and modify the chemical composition and surface features of stalks through Fe-oxyhydroxide mineralization. The carbon content of the stalks was generally indistinguishable from background levels, suggesting that organic compounds were either scarce initially or lost due to percolating hydrothermal fluids. Dendrites and thicker abiotic filaments from a nearby chimney were composed of nanometer-sized microcrystalline iron particles and silica and showed Fe growth bands indicative of inorganic precipitation. Our study suggests that the identification of fossil stalks and sheaths of Fe-oxidizing bacteria in hydrothermal paleoenvironments may not rely on the detection of organic carbon and demonstrates that abiogenic

filaments differ from stalks and sheaths of Fe-oxidizing bacteria with respect to width distribution, ultrastructure, and textural context.

KEYWORDS

biomineralization, biosignature, Fe-oxidizing bacteria, microbial textures, twisted stalks

1 | INTRODUCTION

Banded iron formations and jaspers record extensive marine deposition of iron in the Precambrian (e.g., Bekker et al., 2010; Klein, 2005). A large proportion of the iron in these deposits occur as oxidized Fe(III), despite the early atmosphere being virtually devoid of oxygen (Lyons, Reinhard, & Planavsky, 2014 and references therein). The exact mechanisms responsible for the precipitation of ferric mineral phases in the early oceans are yet to be established, but microorganisms have been suggested to facilitate Fe(II) oxidation (Chi Fru et al., 2013; Holm, 1987; Kappler, Pasquero, Konhauser, & Newman, 2005; Konhauser et al., 2002; Planavsky et al., 2009). Microaerophilic neutrophilic Fe-oxidizing bacteria thrive in suboxic conditions and may have contributed to the generation of iron deposits after the Great Oxidation Event in the Palaeoproterozoic (Chan, Emerson, & Luther, 2016; Crosby, Bailey, & Sharma, 2014; Planavsky et al., 2009; Slack, Grenne, & Bekker, 2009; Slack, Grenne, Bekker, Rouxel, & Lindberg, 2007), or possibly even earlier in the Earth's history (Dodd et al., 2017). The metabolic byproducts of microbial microaerophilic Fe(II) oxidation are extracellular Fe(III)-oxyhydroxide stalks, which are easily recognizable because of their distinct twisted and branching morphologies (Ghiorse, 1984). The morphological uniqueness and the direct connection between twisting and branching traits and fundamental cell behavior, that is, motility and cell division, make the extracellular stalks ideal biosignatures of microbial Fe oxidation in the rock record (Chan, Fakra, Emerson, Fleming, & Edwards, 2011). As the stalk-forming Fe oxidizers are highly sensitive to O₂ concentrations and therefore require a strong redox gradient for growth, the stalks also function as palaeo-environmental indicators (Krepeski, Emerson, Hredzak-Showalter, Luther, & Chan, 2013). Communities of Fe-oxidizing bacteria produce organized microbial mats, which are characterized by directional filamentous textures and alternating sparsely and strongly mineralized bands, reflecting the flux of key substrates and the prevailing hydrodynamic conditions (Chan, McAllister, et al., 2016).

Fe-oxyhydroxide deposits in modern low-temperature hydrothermal environments on the seafloor commonly host Fe-oxidizing Zetaproteobacteria (e.g., Emerson & Moyer, 2002; Forget, Murdock, & Juniper, 2010; Kato, Kobayashi, Kakegawa, & Yamagishi, 2009; Li et al., 2012; McAllister et al., 2019; Scott, Breier, Luther, & Emerson, 2015), which actively contribute to the growth of the deposits through biomineralization and stalk formation (e.g., Alt, 1988; Boyd & Scott, 2001; Edwards et al., 2011; Juniper & Fouquet, 1988; Karl, Brittain, & Tilbrook, 1989; Kennedy, Scott, & Ferris, 2003; Langley et al., 2009). These deposits may be similar to the sedimentary

precursors of jaspers and iron formations, both with respect to mineralogy and genesis. Silicified hydrothermal Fe-oxyhydroxide precipitates are particularly valuable as analogues for ancient Fe deposits because biominerals produced by Fe-oxidizing bacteria have a higher potential for preservation when encased in silica. Compelling examples of biogenic stalks with characteristic twisted and hollow morphologies have been reported from modern, silicified hydrothermal deposits (Dekov et al., 2015; Sun et al., 2015, 2012) as well as from ophiolite-hosted Proterozoic and Phanerozoic jaspers (Boyce, Little, & Russell, 2003; Duhig, Davidson, & Stolz, 1992; Little, Glynn, & Mills, 2004; Little & Thorseth, 2002), suggesting that microbial Fe oxidation has remained an essential process in hydrothermal environments over a protracted period of geological time. Other than twisted morphology, biosignatures that have been advanced for microaerophilic Fe-oxidizing bacteria in the rock record include: constant filament widths, narrow width distributions, strong filament directionality, filament direction changes, bending, and bifurcation (Chan et al., 2011; Hofmann, Farmer, Blanckenburg, & Fallick, 2008; Krepeski et al., 2013). However, the morphologically and texturally based identification of Fe-oxidizing bacterial remains is far from unambiguous. Over time, seafloor Fe deposits typically experience diagenetic recrystallization, which obscures the distinct twisted and branching morphological traits that link filament growth to biomineralization by Fe-oxidizing bacteria. Furthermore, abiotic processes have been advocated to explain some of the common textural features in hydrothermal Si-Fe deposits, including dendrites and moss agates (Hopkinson, Roberts, Herrington, & Wilkinson, 1998; Little et al., 2004) and twisted and striated silica filaments (Park, Lee, Cheon, & Park, 2001; Sokolev & Kievsky, 2005), as well as tubes with particulate iron interiors (García-Ruiz, Nakouzi, Kotopoulou, Tamborrino, & Steinbock, 2017) have been generated experimentally by using entirely abiotic processes. Thus, one of the key remaining challenges in the search for microbial Fe oxidation in the rock record is to confidently distinguish true iron biominerals, from abiotic chemical precipitates, in Fe deposits that have experienced diagenetic alteration.

The Jan Mayen Vent Fields (JMVF), located along the southernmost segment of the Mohns Ridge, comprise both actively forming low-temperature Fe-oxyhydroxide deposits (Johannessen et al., 2017; Moeller et al., 2014; Pedersen, Thorseth, Nygård, Lilley, & Kelley, 2010; Vander Roost, Thorseth, & Dahle, 2017) and extinct chimneys and mounds characterized by interlayered silica and siliceous Fe-oxyhydroxides. Molecular work conducted on the active, low-temperature portion of the JMVF has revealed a high abundance of Zetaproteobacteria, including the stalk-forming Fe-oxidizing bacterium *Mariprofundus ferrooxydans*, suggesting

that microbial Fe oxidation plays a key role in the formation of the Fe-oxyhydroxide deposits (Johannessen et al., 2017; Vander Roost et al., 2017). The association of deposits with different silica contents provides a unique opportunity to study early taphonomic processes and improve the understanding of how extracellular Fe-oxyhydroxide stalks are preserved with time. The Si-Fe deposits from the extinct field at the JMV are ideal targets for reevaluating the robustness of morphological biosignatures, because their excellent preservation aids in the identification of stalks produced by Fe-oxyhydroxide biomineralization. Furthermore, these deposits are formed in a natural hydrothermal environment similar to the inferred depositional setting of Phanerozoic and Proterozoic jaspers (e.g., the Løkken Jasper; Grenne & Slack, 2003) and have experienced silicification and early diagenetic alteration. Through textural analyses and focused ion beam preparation of filament cross sections from the extinct Si-Fe mounds and chimneys, we aim to document how early seafloor diagenesis and silicification affect the ultrastructure and chemical composition of extracellular stalks and how microfossils of Fe-oxidizing bacteria can be distinguished from fossil-like abiotic precipitates.

2 | MATERIALS AND METHODS

2.1 | Geological setting and sampling

The Troll Wall forms the northernmost hydrothermal field within the Jan Mayen Vent Fields and is located at 71°N and 6°W along the southwestern segment of the ultraslow-spreading Mohns Ridge in the Norwegian-Greenland Sea (Figure 1a). Active venting of 270°C warm, white smoker-type fluids takes place along the fault-bounded margin of a rift that transects the axial volcanic ridge (Pedersen et al., 2010). Extensive areas in the center of the rift are dominated by diffuse, low-temperature venting and microbially mediated deposition of laminated, siliceous Fe-oxyhydroxides and Mn oxides (Johannessen et al., 2017; Moeller et al., 2014). An extinct vent field was discovered ca. 500 m east of the active hydrothermal field in 2011. The extinct field is situated on the crest of the axial volcanic ridge at a depth of ca. 460 mbsl and hosts laminated mounds and columnar chimneys composed of silica and Fe-oxyhydroxides (Figure 1b–e). These mound and chimney deposits were sampled by a remotely operated vehicle (ROV) during cruise with R/V G.O. Sars in 2011 and 2012. Mound samples were retrieved by using a shuffle box with a shovel front. The Si-Fe chimney was sliced with a chain saw and collected using the robotic arm of the ROV. Samples were air-dried on board after recovery.

2.2 | Petrographic microscopy

Sample fragments were embedded in epoxy, and thin sections were prepared following standard procedures. The thin sections were studied under a Nikon Eclipse LV100 polarizing microscope located at the University of Bergen, Norway. Images were

obtained by a DS-Fi1 color camera connected to the NIS-Elements BR 2.30 software.

Areas with abundant filaments were selected for analysis of width distribution and were photographed under 200X magnification in plane-polarized light. Filament widths were measured from thin section images using the ImageJ software. For selection of filaments for width measurements, a 10 x 10 grid was superimposed on the image. Measurements were undertaken while moving progressively from left to right between the horizontal lines. All filaments intersecting the vertical lines of the grid were included in the analysis and were measured along segments residing in the plane of focus.

One optical photomicrograph of the Si-Fe mound sample and one image of the chimney sample were selected for directionality analysis. Both showed filaments with apparent preferred orientation. The orientation distribution was measured using the local gradient approach of the Directionality plugin in ImageJ (developed by Dr. Jean-Yves Tinevez). Orientations ranging from -90° to 90° were recorded and the results were grouped into 90 bins of 2° each.

2.3 | Scanning electron microscopy (SEM)

Textures and detailed morphology of individual filaments were studied using a Zeiss Supra 55VP Field Emission Scanning Electron Microscope (FE-SEM) at the University of Bergen. Prior to analysis, thin sections were coated with C using an Agar Turbo Carbon Coater. Mound and chimney fragments were attached to Al stubs and coated with Ir using a Gatan 682 Precision etching coating system. Thin sections were studied in backscatter electron (BSE) mode, and phases were identified with a Thermo Noran Six Energy Dispersive Spectrometer (EDS). Analyses were performed at a voltage of 15 kV and a working distance of 8 mm. Mound fragments were investigated by using the secondary electron (SE) detector at 5 kV and with an average working distance of 3 mm. The SEM was used to preselect individual filaments for focused ion beam preparation of thin section samples. Intact filaments located in depressions of the thin section were preferred targets.

2.4 | Focused ion beam-transmission electron microscopy (FIB-TEM)

Focused ion beam (FIB) preparation of samples for transmission electron microscopy (TEM) analysis was performed at the NTNU NanoLab in Trondheim, Norway. Prior to FIB milling, thin sections were coated with a ca. 30-nm-thick layer of Au. Cross sections of targeted filaments were cut perpendicular to their long axis using a FEI Helios NanoLab 600 DualBeam FIB-SEM. Protective layers of Pt (e-beam assisted deposition) and C (ion-beam assisted deposition) were deposited on the surface of the selected area prior to milling, and the material on each side of the protective strip was removed by sputtering, leaving a sample with a size of approximately 10 x 15 x 3 μm. The FIB sample was transferred and welded to a Cu TEM-grid with a W Omniprobe lift-out needle and subsequently thinned to approximately 100 nm. Coarse thinning

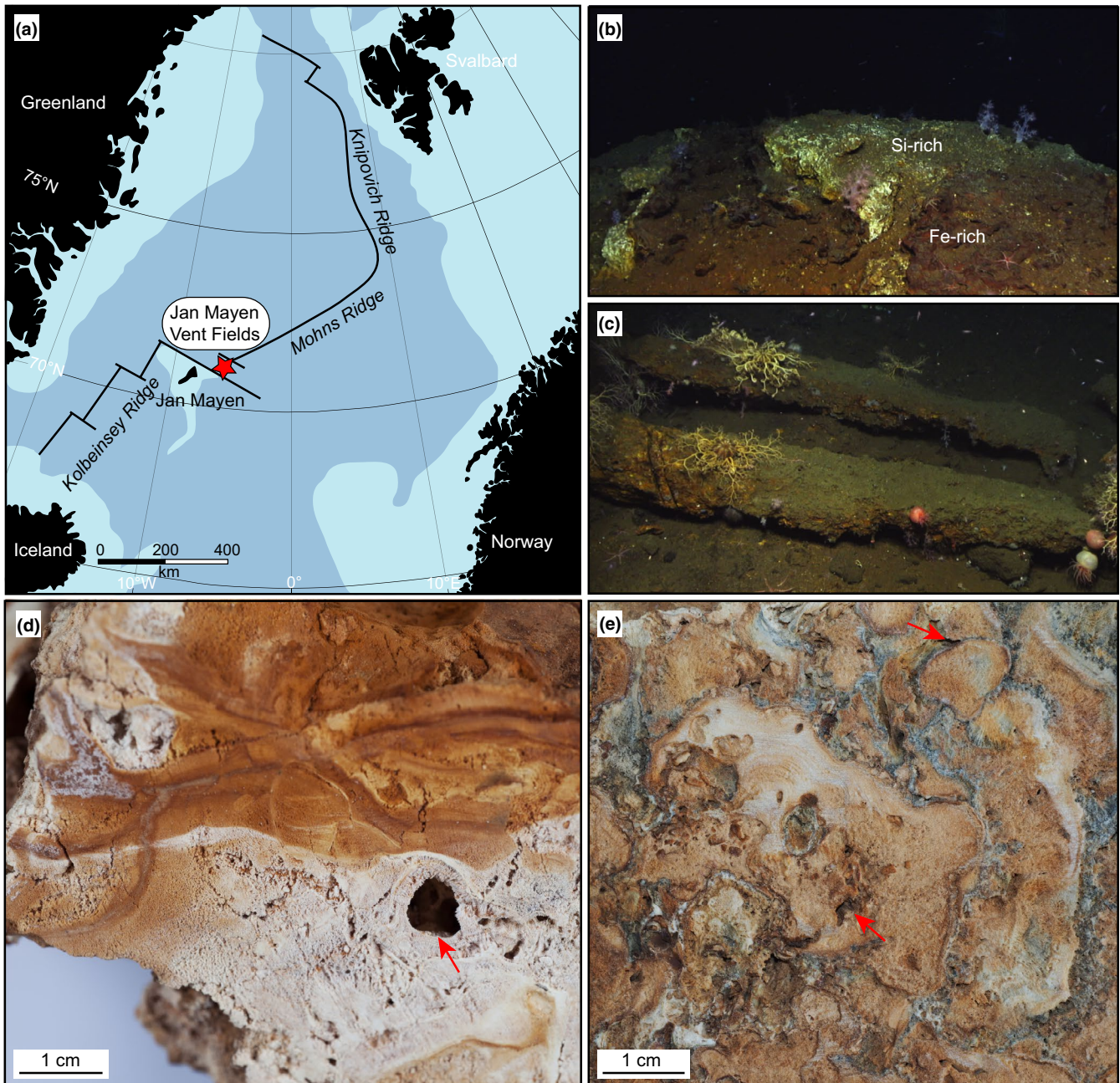


FIGURE 1 Si-Fe deposits sampled at the Jan Mayen Vent Fields. (a) Location of the Jan Mayen Vent Fields along the southern Mohns Ridge in the Norwegian-Greenland Sea. (b) ROV image of extinct silica-iron mound. (c) ROV image of two tipped-over silica chimneys with lengths of approximately 2 m. (d) Sampled laminated mound fragment. Red arrow points to cavity. Fe-rich (rusty brown), silica-rich (white), and intermediate (light brown) laminae were studied. (e) Sampled chimney fragment. Red arrows point to crevasses

was performed at 30 kV acceleration voltage, while the final thinning was performed at 5 kV.

Transmission electron microscopy characterization was performed with a double Cs-corrected cold-FEG JEOL ARM 200CF, operated at 200 kV and equipped with a 100 mm² (0.98 sr solid angle) Centurio SDD for energy dispersive X-ray spectroscopy (EDS). In order to remove surficial hydrocarbons from the samples, the FIB foils were gently plasma cleaned with a shielding holder in a gas

mixture of 75% Ar and 25% O₂ for 30 s prior to analysis. Electron diffraction was performed on both Fe-rich and Si-rich phases to determine crystallinity. Elemental compositions were measured by EDS. The EDS maps were processed in MatLab using the jet color scale from dark blue to dark red with matrix values adapted to the intensity of each set of maps. Images were acquired in both TEM and STEM modes. Minimum and maximum filament diameters were measured using the ImageJ software.

3 | RESULTS

3.1 | Sample architecture

3.1.1 | Laminated Si-Fe mound

The sample fragments from the Si-Fe mounds showed irregular, nodular geometry and displayed clearly defined Si- and Fe-rich layers (Figure 1d). Each layer was composed of a series of microscopic laminae. Internal layers were primarily composed of fibrous silica with local bands of massive silica. The outer parts of the sample fragments consisted of laminated Fe-rich precipitates with alternating porous and densely mineralized textures. Aligned fibers were evident in some Fe-rich parts of the hand specimen. Small internal cavities were locally present and were particularly prominent in the silica-rich layers (see Figure 1d).

3.1.2 | Si-Fe chimney

The chimney fragments were composed of consolidated, yet porous material and lacked systematic layering showing an apparently random distribution of intermixed silica and Fe-rich precipitates (Figure 1e). Large channels and concentric layers were not observed, but smaller cavities and crevasses, ranging in size from <1 to 5 mm in diameter, were abundant and could locally be traced from the base to the top of the sample fragment (see Figure 1e). Clusters of channels were evident in some areas and alternated with denser fibrous textures and massive silica-rich domains.

3.2 | Textures

3.2.1 | Laminated Si-Fe mound

Optical microscopy and BSE-SEM of thin sections from the Si-Fe mounds revealed alternating Fe-rich and silica-rich laminae with complex filamentous and banded textures. Three main, morphologically distinct filament types were evident in Fe-rich laminae (Figure 2). These filament types were typically confined to separate areas, but were locally found to co-occur. The most prevalent filamentous texture comprised clusters of irregular, gently curved, and branching filaments showing semi-parallel or radiating orientation over lateral distances of <2–3 mm (Figure 2a). The filaments were locally associated with directional dendritic features, measuring 500–1,000 μm across and ca. 500–1,500 μm in the branching direction (Figure 3). BSE-SEM demonstrated that the dendrites were composed of dispersive and radially growing filaments, some of which possessed indications of twisting (Figure 3h). Networks of randomly oriented, narrow, straight filaments appeared to be nearly equally abundant as the irregular forms (Figure 2c), but the two morphotypes were largely confined to separate laminae. Branching did not appear to be a ubiquitous trait associated with the straight morphology, but the filaments were found to attach to other straight filaments, constructing complex networks (Figure S1a). Irregular,

curved filaments were commonly minor components in domains dominated by straight, randomly oriented filaments, while the opposite association was less frequently observed. Shorter single and multiple branching filaments were present along with both the irregular and straight forms (Figure 2e), and their trunks were typically attached to neighboring filaments. Fe-rich precipitates lacking clearly discernible structure were present in variable amounts on the surfaces of all filament morphotypes. Heavy Fe mineralization partly obscured the filamentous fabric in some areas. Fe-rich bands, ranging in thickness from 5 μm to several mm, were evident in the interface between domains of different texture. The Fe-rich bands locally occurred as stacked, dome-shaped structures (Figure S1b). Irregular, curved, and branching filaments were visible in the least Fe-rich portions of the bands.

SEM analysis of Fe-rich sample fragments of the laminated mounds revealed a high abundance of ribbon-like twisted stalks mineralized to variable extent by globular Fe precipitates (Figure 2b; Figure S2 and Figure S3a–d). Straight, narrow filaments with hollow interiors (Figure 2d; Figure S1c) were also common and occurred together with branching, hollow tubes with elongated cross sections, and striated external surfaces (Figure 2f; Figure S3e–f). Silica was commonly present interstitially as pitted flakes (see Figure 2d,f) and was locally encrusting Fe-rich filaments. The extent of silica mineralization appeared to increase toward silica-rich laminae, from interstitial precipitates via <100-nm-thick, pitted crusts and >1- μm -thick, bulbous casts to massive domains where filaments were fully embedded in silica (see Figure 2b).

Silica-rich laminae were mainly composed of wide, straight silica filaments, which were lacking Fe-rich cores (Figure 2g; Figure S4). These filaments showed strong directionality across distances of more than 2–3 mm, generating hair-like fabric (Figure S4f). The filamentous fabric locally graded into bands of massive silica. SEM confirmed that large areas of the silica-rich sample fragments were composed of aligned, ca. 2- to 15- μm -wide, hollow tubes with wall thicknesses varying from ca. 200 nm to 2 μm (Figure 2h). Cross sections of individual tubes were found in the massive silica bands.

3.2.2 | Si-Fe chimney

The textures in the Si-Fe chimney samples differed from the mound textures with respect to the size, directionality, and morphology of filamentous features. Major parts of the chimney samples were composed of radially oriented, semi-linear filaments intersected by narrower, orthogonal filaments that appeared to outline arcs (Figure 4a; Figure S5). The radial filaments were composed of silica with cores of Fe-rich, particulate material and showed local branching, which increased in intensity toward 10- to 100- μm -wide, silicified, Fe-rich bands and dendrites (Figure 4b–d). Multiple branching filaments and dendrites displayed decreasing interstitial space between branches and locally orthogonally oriented bands of decreasing Fe content in the direction of growth (see Figure 4c).

Scanning electron microscopy confirmed the presence of several hundred micrometer long, branching silica filaments, locally showing

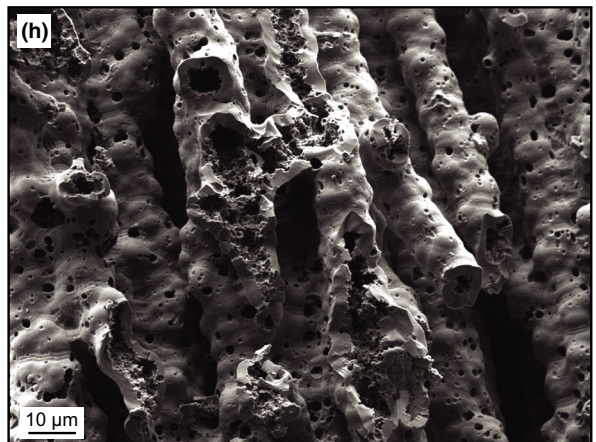
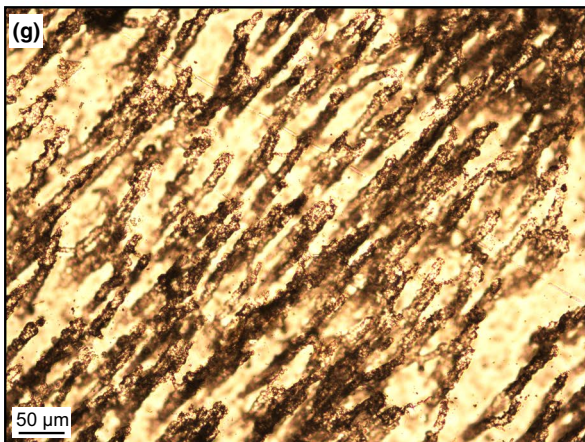
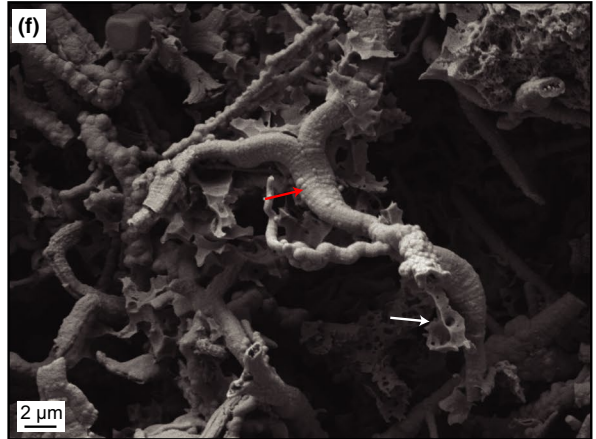
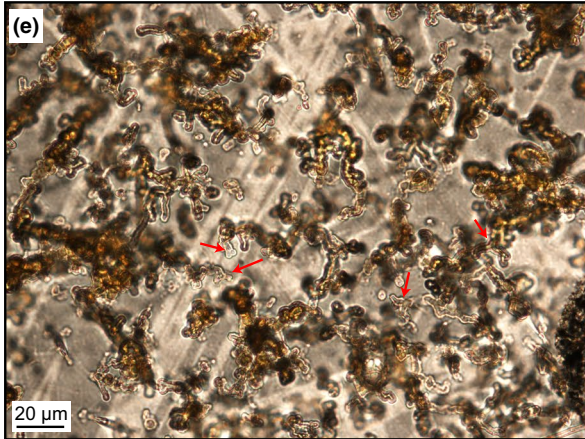
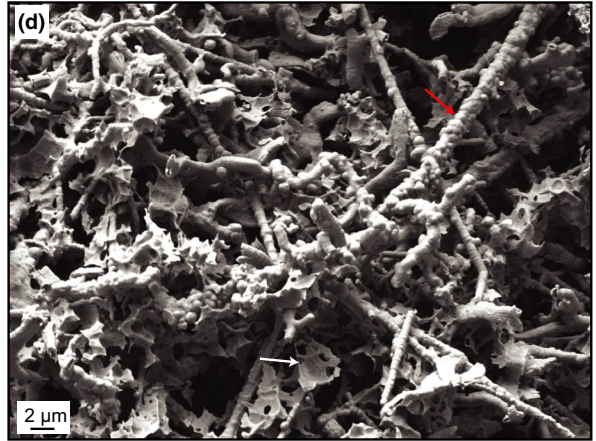
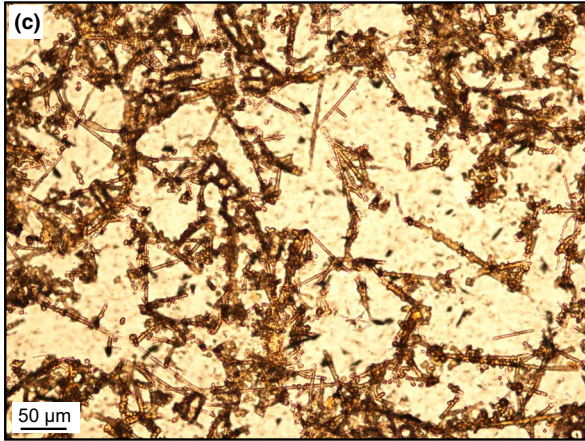


FIGURE 2 Optical micrographs (left) and SEM images (right) of filaments in the Jan Mayen Si-Fe mound. (a) Narrow, irregular filaments showing apparent preferred orientation and local branching. Arrows indicate twisted morphologies. (b) Twisted filament embedded in silica. Filament cross sections are evident in the upper left and lower right corners (arrows). (c) Narrow, straight, randomly oriented filaments. (d) Narrow, straight filaments (red arrow) and branching filaments mineralized to variable extents. The pitted flakes (white arrow) are thin silica casts. (e) Branching curvilinear filaments (red arrows). (f) Tubular, branching filaments (red arrow) and additional straight filaments mineralized by globular precipitates and pitted silica flakes (white arrow). (g) Strongly aligned, wide filaments in Si-rich layer. (h) Aligned silica tubes

remarkably consistent directionality (Figure 4e). Both filaments with solid and porous interiors were evident. Botryoidal silica surfaces were visible within some pore spaces (Figure 4f). Tabular planes composed of closely spaced silica strands were locally found at high angle to the main set of branching filaments (see Figure 4e). These planes were strongly mineralized by botryoidal silica. Fe-rich globular aggregates and fibrillar precipitates were evident on the surfaces of silica filaments in some areas, locally forming rounded nests and ca. 5- to 10- μm -wide, hollow tubes with porous, fibrillar walls (Figure 4g-h, Figure S6).

3.3 | Widths and directionality of filaments

The widths of the three most prominent filament types in the Fe-oxyhydroxide mound samples were measured and the distribution analyzed (Figure 5a). Owing to the inconsistent occurrence of the short branching form (Figure 2e,f), filaments with this morphology were not assigned a separate category. The widths of the irregularly curved, aligned filaments (Figure 2a) ranged from 1.32 to 12.42 μm , with a median value of 3.37 μm . Thin, straight filaments (Figure 2c) showed a narrower size range and slightly smaller diameters, ranging from 1.33 to 10.45 μm , with a median value of 3.26 μm . Parallel, long silica filaments (Figure 2g) were significantly wider than the two other forms, displaying diameters of 4.34–22.22 μm , with a median value of 10.71 μm . The maximum and minimum diameters of Fe-rich filament cross sections in the FIB-TEM images (Figure S7) were in the range of 1.14–2.35 μm , with a median of 1.70 μm . Filaments in the chimney showed clearly distinguishable Fe-rich cores with diameters ranging from 1.49 to 22.93 μm and a median value of 8.77 μm (Figure 5b). The iron-rich central regions were encrusted by silica casings. Total filament widths including silica crusts ranged from 12.16 to 41.93 μm , with a median of 24.25 μm .

The directionality of filaments in the laminated mound fragments varied between laminae. Poorly ordered textures were commonly associated with narrow, straight filaments, and directional textures were observed in laminae where the irregular morphotype predominated. The image selected for analysis showed irregular, gently curved Fe filaments with preferred orientation (Figure 5c). This particular image was chosen to compare aligned fabric in the mound and chimney samples. The directionality analysis revealed a good Gaussian fit (0.99) with a standard deviation of 31°. At least 45% of the filaments showed similar orientation. The directionality data from the chimney image (Figure 5d) displayed a good fit to the Gaussian distribution (0.99) and a standard deviation of 23°. At least 75% of the filaments showed similar orientation.

3.4 | Internal ultrastructure and chemical composition

FIB-TEM of selected irregular filaments in the mound samples from the Jan Mayen Vent Fields revealed surprisingly complex ultrastructure and elemental distribution. All studied filaments displayed concentrically laminated cores composed of an amorphous, siliceous Fe phase (see Figure S8b for diffraction data). Four out of eight of the studied filament cross sections showed distinct, homogeneous innermost core regions with high-porosity central parts (Figure 6, Figure S7). P was particularly enriched in the outer part of the core in filaments with this particular ultrastructure. The concentric laminae enclosing the innermost core showed granular textures and inter-laminar variations in the concentrations of Si, P, S, C, and N (Figure S8). Elevated C concentrations were only detected in the concentric laminae of one filament (see Figure 6e). The C enrichment could be traced from the laminae through a crack in the silica encrusting the Fe-rich filament. One filament cross section showed distinctly larger central pores fringed by Si-rich precipitates (Figure 7). All studied Fe-rich filaments were encrusted by >1- μm -thick layers of massive, amorphous silica.

The wide filaments in the chimney samples were primarily composed of amorphous silica, but displayed cores with disconnected voids and dispersed globular precipitates composed of amorphous silica and minor Fe (Figure 8). Fe-rich crystalline bands were evident in the center of some particles (Figure 8d,e). The lattice fringe spacing of the crystalline phase, determined from TEM images, was 2.2 Å. Within the accuracy of the measurement, this spacing is consistent with the crystal structures of hematite (rhombohedral Fe_2O_3 where $d_{113} = 2.21$ Å), goethite (orthorhombic $\text{FeO}(\text{OH})$ where $d_{401} = 2.18$ Å, $d_{102} = 2.23$ Å, and $d_{211} = 2.24$ Å) and wüstite (face-centered cubic FeO where $d_{200} = 2.15$ Å). The crystalline bands were rapidly obliterated under the electron beam, indicating weak bonds between the layer structures. Goethite thus appears to be the most likely candidate, although our current data do not allow conclusive identification of the crystalline phase.

4 | DISCUSSION

4.1 | Fe-oxyhydroxide filaments in laminated Si-Fe mounds—testing the biogenicity of different morphotypes

Our data have revealed several different filament morphotypes in the JMVF mounds: twisted stalks, straight narrow filaments, short branching filaments, and thick parallel silica filaments. We now

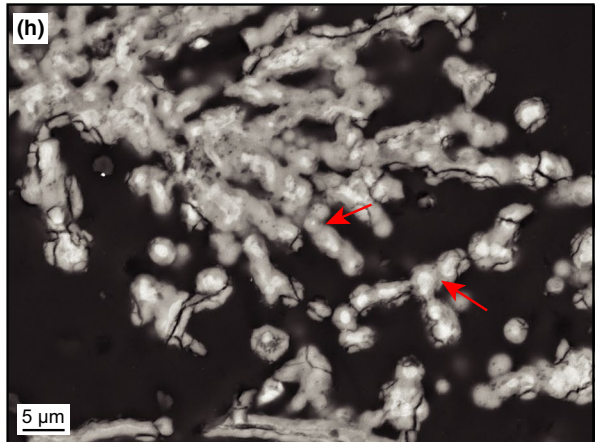
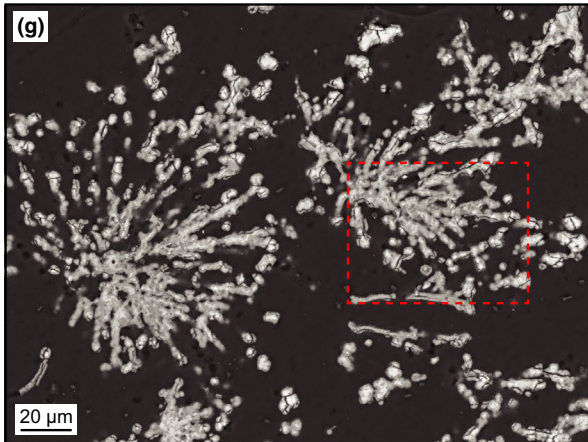
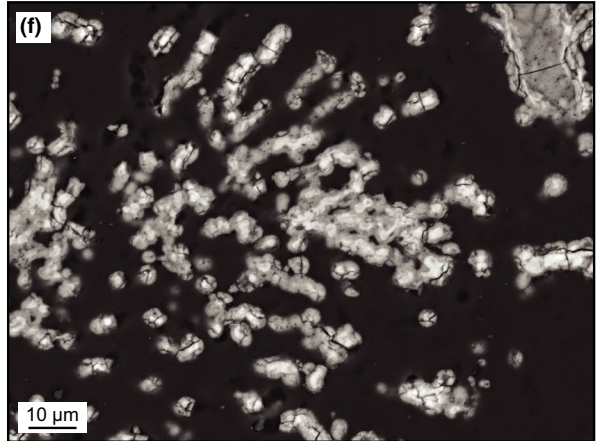
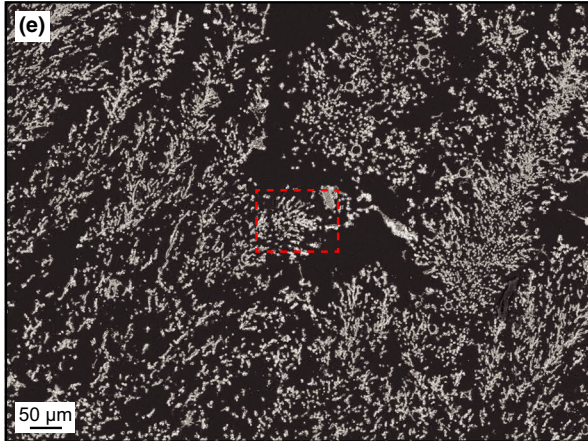
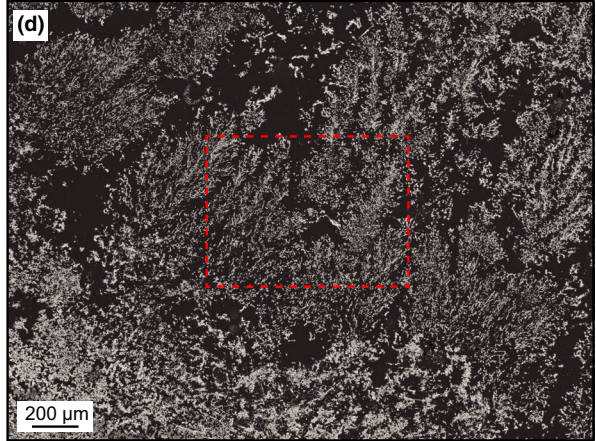
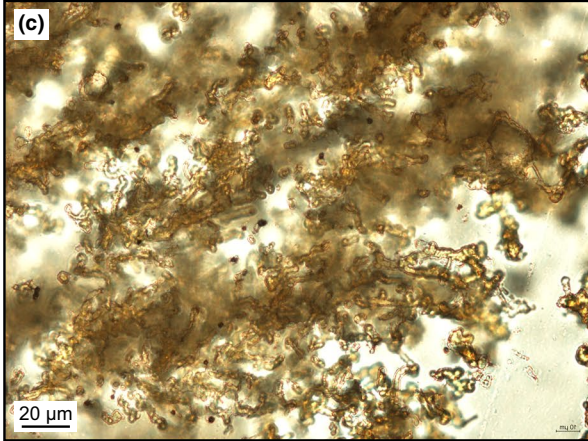
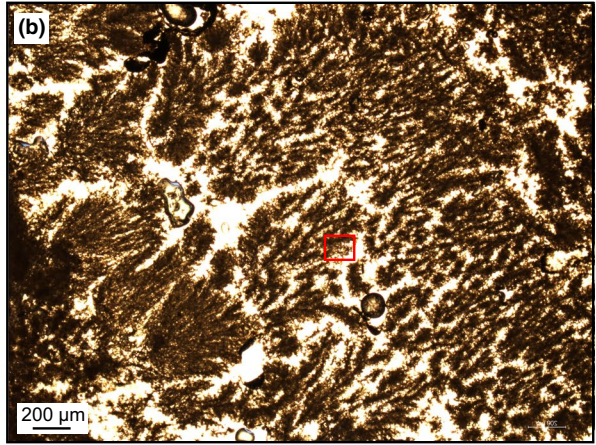
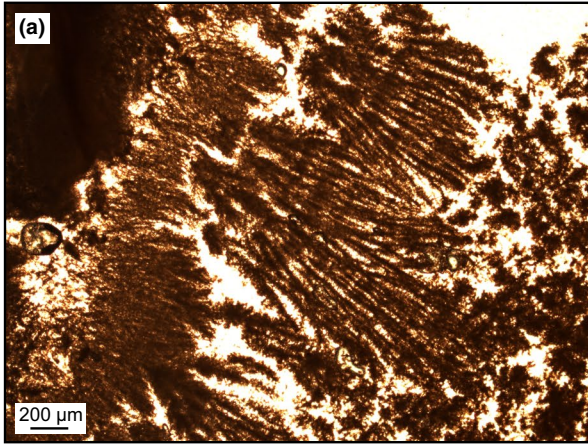


FIGURE 3 Mound dendrites. (a–b) Optical microscope overview images of dendritic features. (c) Part of dendritic feature in B under higher magnification (location shown by red box in b). The branches are composed of clusters of curved filaments. (d) Backscatter electron SEM (BSE SEM) overview image of dendrites. (e) Higher magnification image of parts of the dendritic features in d (location shown by red box in d). (f) Higher magnification image of one of the dendrite branches in e (location shown by red box in e). The light gray phase in central parts of the filaments is Fe-rich, the encrusting darker gray phase is silica, and the surrounding black material is epoxy resin used for mounting. (g) Radial features composed of filaments. (h) Higher magnification image of the feature in g (location shown by red box in g). Arrows point to filaments that display indications of twisting (note the distribution of the light gray, Fe-bearing phase)

discuss which filament morphotypes are most likely biogenic and link surface and interior ultrastructure evident through combined SEM and FIB-TEM with observations of the filamentous textures by optical microscopy.

The twisted stalk morphology is considered to be a diagnostic feature of the Fe oxidizers *Mariprofundus ferrooxydans* and *Gallionella ferruginea* (e.g., Chan et al., 2011; Comolli, Luef, & Chan, 2011; Emerson & Moyer, 2002). However, compelling twisted specimens have only been recognized in a handful of samples from modern and Phanerozoic hydrothermal Si-Fe deposits (e.g., Boyce et al., 2003; Little et al., 2004; Sun et al., 2015). In our Jan Mayen Si-Fe mound samples twisted stalks were clearly identified in large numbers by our SEM investigations (Figure S2), but unmistakably twisted filaments were surprisingly rare in thin sections. Individual examples of twisted stalks were found among less distinctly shaped irregularly curved filaments (Figure 2a). The irregular form shares several traits with the twisted stalks, including directional growth and sinuous margins. Considering the high abundance of irregular filaments in both sample fragments and thin section and the spiral-like shape outlined by the distribution of Fe in BSE-SEM (see Figure 3h), we infer that this morphotype is a common 2D expression of twisted stalks.

The widths of fresh extracellular stalks of *Mariprofundus ferrooxydans* are reported to range from 0.6 to 2.2 μm (e.g., Krepski et al., 2013). In comparison, the median width of the irregularly aligned filaments from the JMVf laminated mound samples is 3.37 μm (Figure 5a). The other morphotypes also show widths that are larger than the typical stalks of Fe-oxidizing bacteria. Larger stalk widths are expected in a natural hydrothermal environment where abiotic Fe-oxyhydroxide precipitation continues after the micro-organism has abandoned the stalk (e.g., Melton, Swanner, Behrens, Schmidt, & Kappler, 2014), but the width distribution may also be influenced by biases introduced during visualization and measuring. Firstly, some stalks are encrusted by thin silica layers, which are difficult to visually identify by optical microscopy and therefore may be included in the measurements. Secondly, measurements of indistinguishable, intergrown filaments may shift the width distribution toward higher values. This problem is particularly prominent in densely mineralized areas of the samples. The filament cross sections studied by FIB-TEM (Figure S7) range in width from ca. 1.1 to 2.4 μm . This range is in accordance with the size data of Krepski et al. (2013).

The directionality and texture of the domains dominated by irregular filaments (Figures 2a and 5c) show striking resemblance to assemblages of stalks produced by *Mariprofundus ferrooxydans* grown in culture in a strong Fe(II)/O₂ gradient (c.f., Krepski et al.,

2013). The standard deviation of the Gaussian fit of the directionality analyses is around 30° for both the Jan Mayen filamentous texture and bands of *Mariprofundus ferrooxydans* stalks, indicating clear directional growth. Krepski et al. (2013) reported directional stalk growth confined to distinct, densely mineralized bands and less ordered textures outside these bands. These results are in good agreement with the optical microscopy results from the Jan Mayen Si-Fe mounds, which show that the preferred orientation of irregular stalks is localized. Microbial mats in natural hydrothermal environments are affected by shifting flow paths and changing redox gradients during progressive Fe-oxyhydroxide precipitation (Chan, McAllister, et al., 2016) and are sporadically exposed to strong fluid flow (Bernis, Lowell, & Farough, 2012). These factors likely impact the directionality of the filamentous fabric by promoting both abrupt and gradual changes in filament orientation, explaining the confinement of aligned filaments to distinct domains. Complex dendritic and radial arrangements of irregular filaments are evident in some of the mound laminae (Figure 3). The distribution of Fe revealed by BSE-SEM (Figure 3c–h) demonstrates that these textural features are composed of silicified twisted stalks. While some Fe-oxidizing species are known to form dendrite-like extracellular structures (Chiu, Kato, McAllister, Field, & Chan, 2017; Edwards, Rogers, Wirsén, & McCollom, 2003), dendritic growth of stalks produced by *Mariprofundus ferrooxydans* or other benthic Zetaproteobacteria has not previously been reported. Twisted stalks have been discovered in association with *Frutaxites*-like iron shrubs in biofilms with active Fe and N-cycling, but were not found to constitute the main framework of these dendrites (Heim, Quéric, Ionescu, Schäfer, & Reitner, 2017). We hypothesize that dendritic and radial filament textures in the JMVf mound deposit form as a response to rapidly shifting redox configurations. Several cells may attach their stalks to a central holdfast to ensure stable positioning in the turbulent flow regime within the mound. Radial stalk growth would minimize competition and maximize the gain of Fe for each cell.

The straight, narrow filament morphotype we identified by optical microscopy (Figure 2c) differs from the twisted stalks of *Mariprofundus ferrooxydans* by its lower sinuosity and smoother surface topography and is morphologically more similar to sheaths of Fe-oxidizing bacteria identified at other vent fields (e.g., Emerson & Moyer, 2002; Fleming et al., 2013; Scott et al., 2015). Straight, hollow tubes reminiscent of extracellular sheaths of marine Fe-oxidizing Zetaproteobacteria and freshwater *Leptothrix ochracea* were also identified by SEM of sample fragments (Figure 2d; Figure S1c). The random textures associated with the straight morphology potentially indicate that the sheath-forming bacterium easily locates

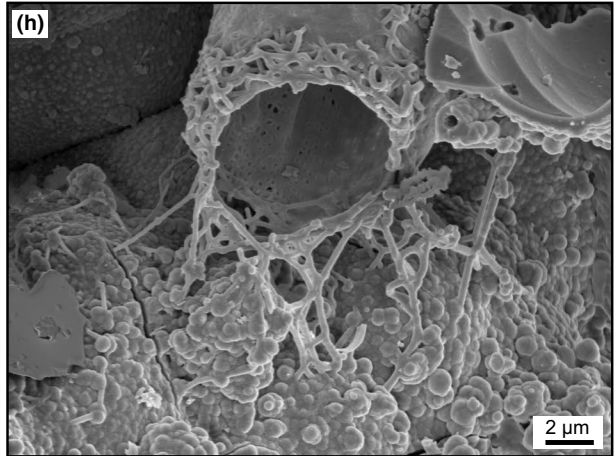
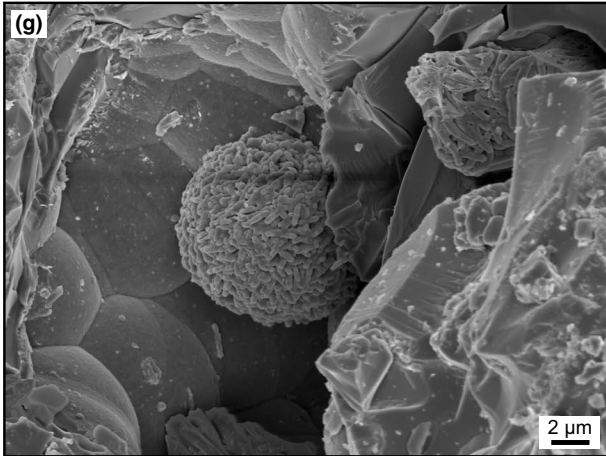
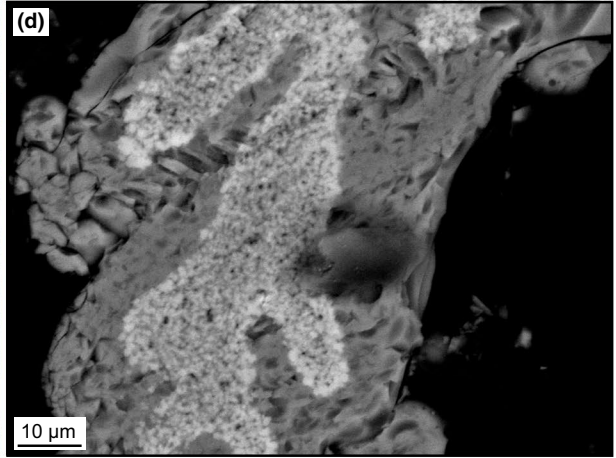
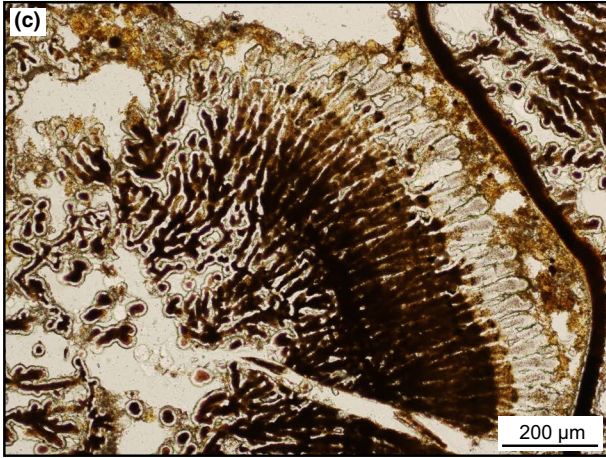
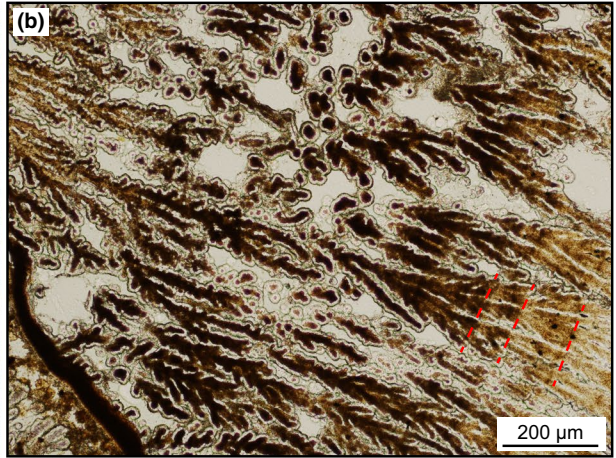
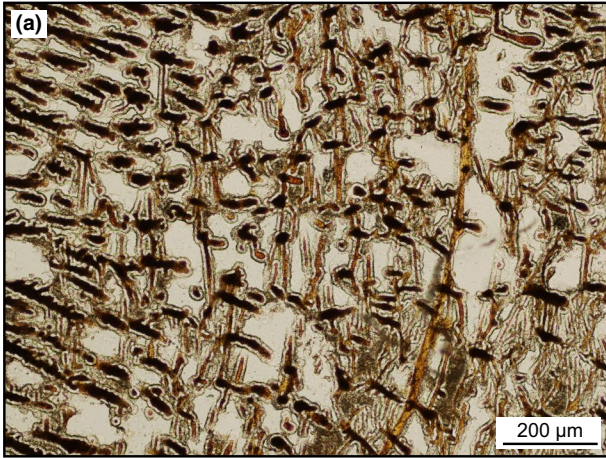


FIGURE 4 Optical micrographs and SEM images of filaments and textures in the Jan Mayen Si-Fe chimney. (a) Strongly directional, wide filaments orientated NW-SE intersected by a set of long, narrower filaments oriented at a high angle to the main set. (b) Multiple branching filaments with stubby branches grading into well-developed dendrites in the lower right of the image. Systematic variations in apparent Fe content are evident in the growth direction (marked by red, stippled lines). (c) Dendrites with marked bands of different Fe content. (d) BSE SEM close-up image of a dendrite branch. Note the particulate texture of the light gray Fe-bearing phase in the center of the branch. The darker gray material is silica, while the black material is epoxy resin used for mounting. (e) SEM image of chimney fragment with parallel, branching silica filaments, interrupted by an orthogonal band of closely spaced silica strings. (f) SEM oblique cross section of bulbous silica filament with porous core. (g) SEM image of an Fe-rich fibrillar, rounded nest with a diameter of ca. 10 μm . (h) SEM image of an Fe-rich tube with fibrillar walls. The diameter of the tube opening is ca. 7 μm

optimal redox conditions and is not required to constantly shift position in response to subtle changes in fluid flow and O_2 availability, unlike the strongly redox-dependent *Mariprofundus ferrooxydans*. At Loihi Seamount, sheath-forming Zetaproteobacteria are abundant in the surface layer of Fe-oxyhydroxide microbial mats and appear to have a higher oxygen tolerance than their stalk-forming counterparts (Chan, McAllister, et al., 2016; Fleming et al., 2013). An analogous ecological relationship has been documented in freshwater Fe seeps (Emerson & Revsbech, 1994; Fleming, Cetinic, Chan, King, & Emerson, 2014). In our JMVf mound samples, different geochemical

requirements between stalk-forming and sheath-forming Fe-oxidizing species could explain why the twisted and straight filamentous forms occur in spatially separate domains.

The short, branching, tubes we identified are easily recognizable in thin section because of their distinct outward-pointing, arborescent branches (Figure 2e). Although this morphology is highly abundant, it does not form distinct domains like the twisted stalks and straight sheaths, but appears infrequently and always co-occurs with the other forms. Branching tubes have been found in a large number of hydrothermal Fe-oxyhydroxide deposits (Boyd & Scott, 2001;

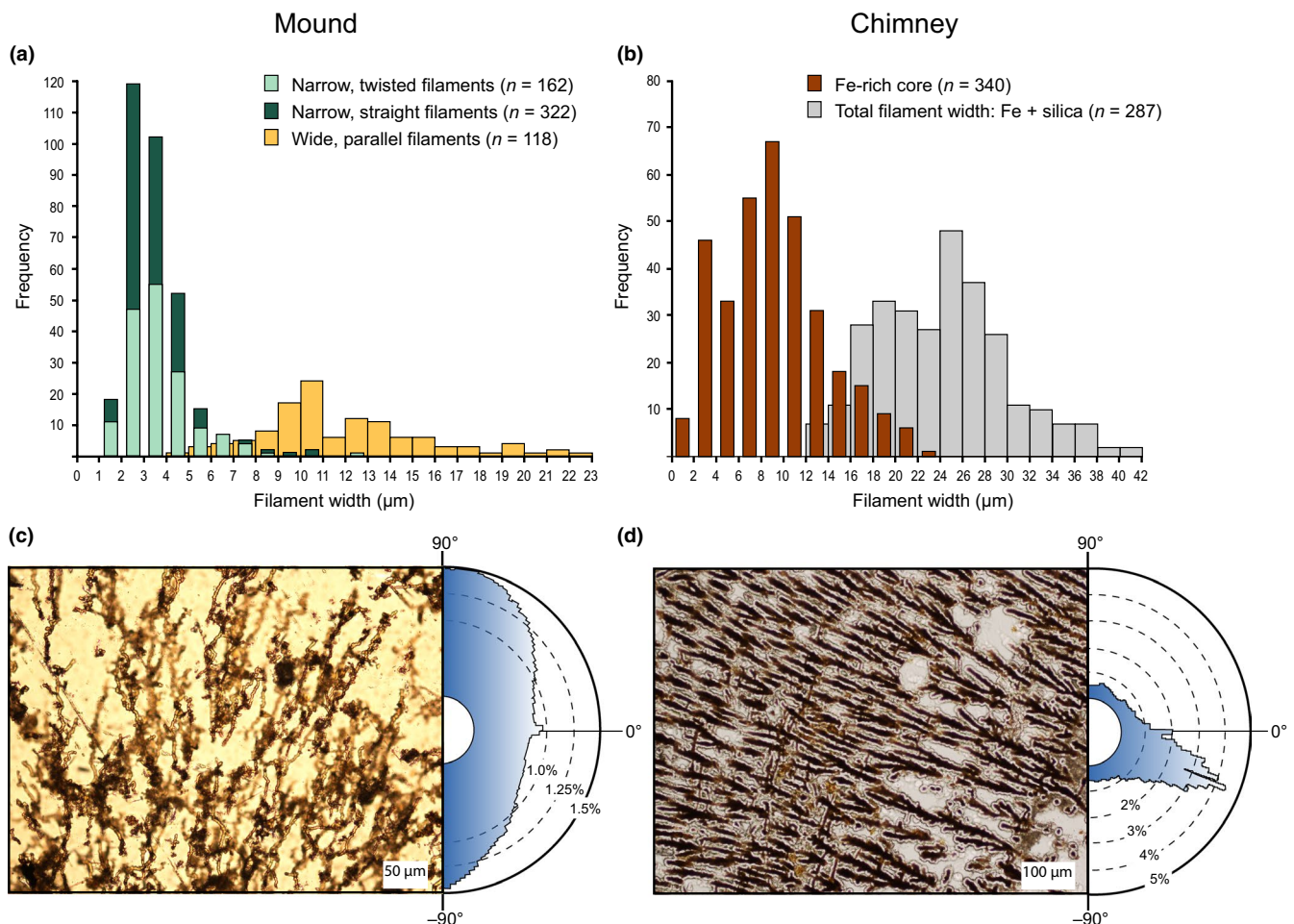


FIGURE 5 Width and orientation histograms: (a) Frequency distribution histograms for filament widths in Si-Fe mound samples. The colors represent the three filament morphotypes presented in Figure 2a, c and g. (b) Frequency distribution histograms for the Fe core and total filament widths in Si-Fe chimney samples. (c) Radial histogram showing the directionality of the narrow, irregular filaments depicted in Figure 2a in a selected image from a Si-Fe mound sample. (d) Radial histogram showing the directionality of the wide, branching filaments in a selected image from a Si-Fe chimney sample

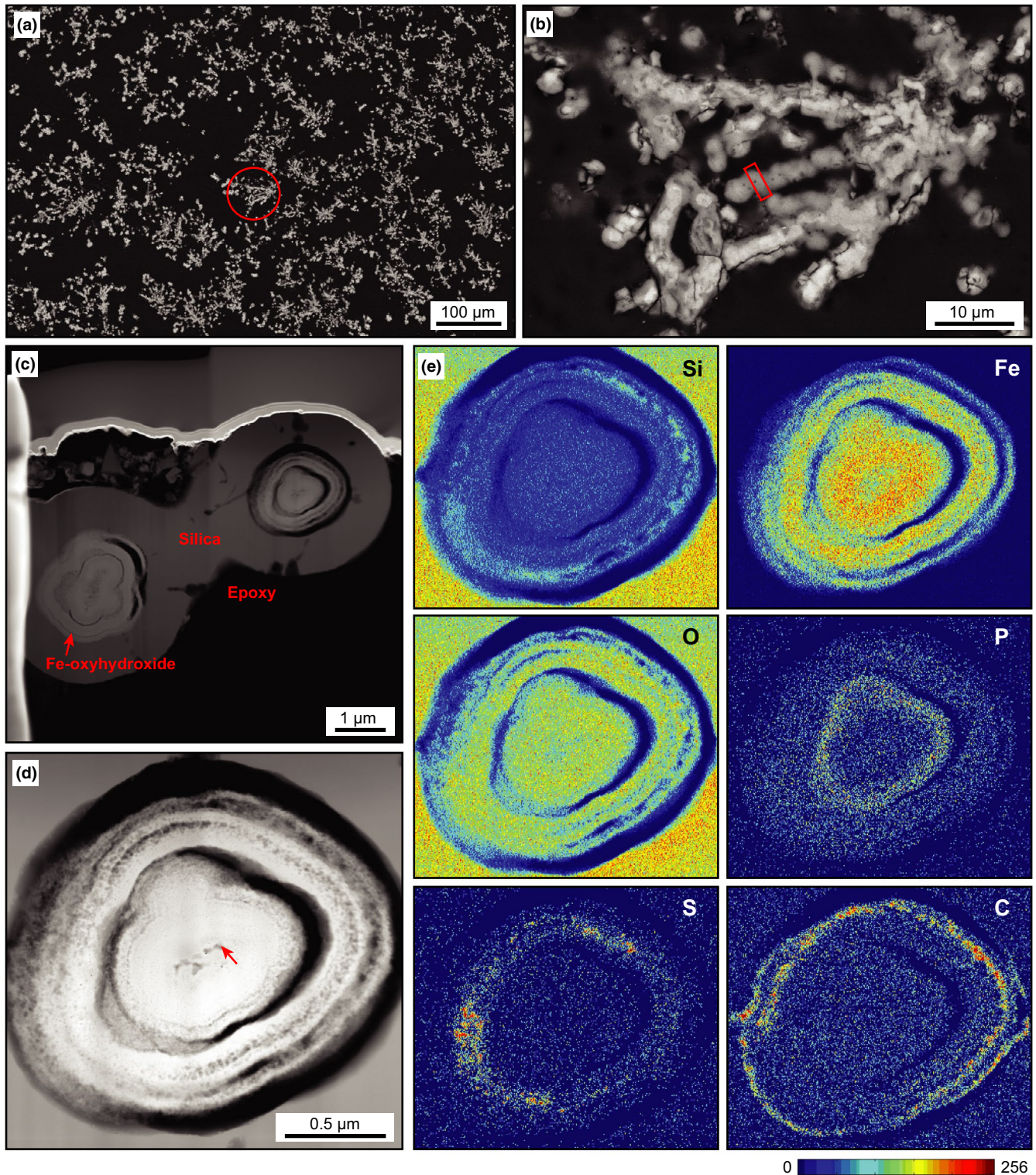


FIGURE 6 Textural context and FIB-TEM data of target filament from the silicified Fe-mound. (a) Backscatter electron SEM image of filaments in thin section. The filament selected for FIB investigation is within the area marked by the red circle. (b) Close-up of the selected filament. The cross section selected for FIB preparation is indicated by a red rectangle. (c) High Angle Annular Dark Field scanning transmission electron microscopy (HAADF STEM) image of the cross section of the target filament also including an additional neighboring filament cross section located below the surface of the thin section. (d) Ultrastructure of the target filament. Red arrow points to central porosity. Pore spaces separating the concentric laminae demonstrate that the filament interior has not been infiltrated by the epoxy resin used for mounting. (e) EDS element maps of the central parts of the filament composed of an Fe-rich core enclosed by homogenous silica. Siliceous Fe precipitates occupy the innermost core region, while the outer core is composed of concentric layers with variable P, C, S, and Si contents. Note that the detection limit for C is approximately 0.1%. The intensity scale ranges from 0 to 256, with blue color representing low element counts and red color representing high element counts

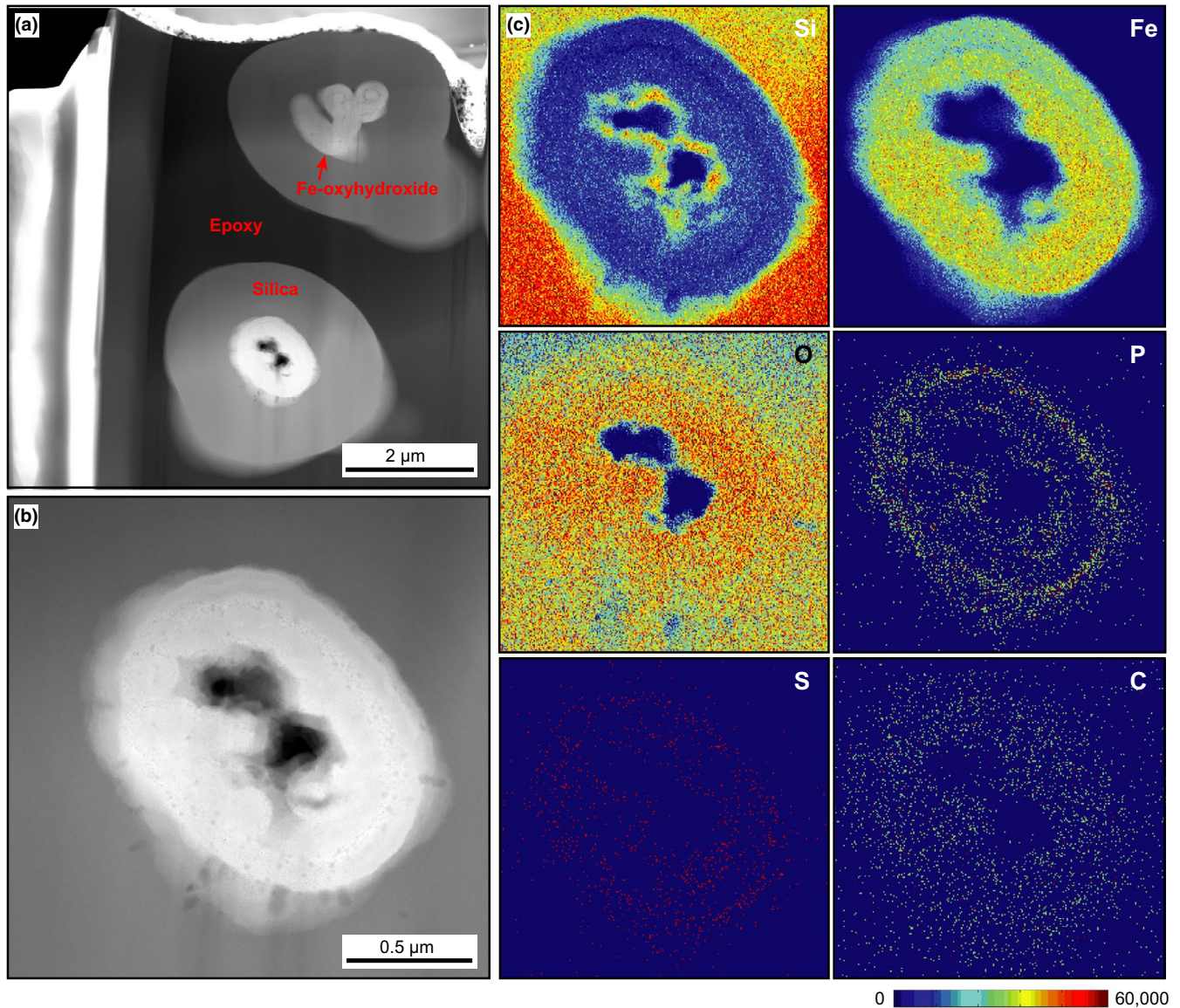


FIGURE 7 TEM of filament cross sections from the silicified Fe-mound. (a) HAADF STEM image of the cross sections of two filaments. The upper feature appears to be composed of two or more distinct filaments, or a strongly curved filament. (b) Close-up of the lower filament, showing a porous innermost core region. (c) EDS element maps of the core of the lower filament. Siliceous precipitates enclose the Fe-rich filament and fringe the pores of the innermost core. P enrichment is localized to distinct concentric bands. The intensity scale ranges from 0 to 60,000

Breier, Gomez-Ibanez, Reddington, Huber, & Emerson, 2012; Chan, McAllister, et al., 2016; Edwards et al., 2011; Emerson & Moyer, 2010; Johannessen et al., 2017; Peng, Ta, Chen, Zhang, & Xu, 2015; Scott et al., 2015) and have been assigned to Zetaproteobacteria through fluorescent in situ hybridization (Emerson, Scott, Leavitt, Fleming, & Moyer, 2017). The relatively short lengths of the tubes, along with their sporadic distribution and attachment to both sheaths and twisted stalks led Chan, McAllister, et al. (2016) to propose that the tube-forming Fe-oxidizing micro-organism is a secondary colonizer adapted to the low O_2 concentrations prevailing at depth in the mat. Our observations of the branching tubes are consistent with this interpretation. Given that tubes, stalks, and sheaths are equally affected by silica encrustation, it would appear that the secondary

colonization of the Fe deposits occurred during the same phase of hydrothermal activity as primary mat construction. The secondary colonizers are likely to be active at depth, while microbial Fe oxidation and biomineralization continue at the surface.

In contrast to the other morphotypes, the thick, parallel tubes found in the silica-rich laminae (Figure 2g,h) show no evidence of Fe-rich core components (Figure S4). The low concentration of Fe either implies that primary Fe-oxyhydroxides were mobilized or obliterated through hydrothermal flow and silicification, or that Fe-oxyhydroxide stalks were never present in the cores of these tubes. Mobilization of Fe would require either complete Fe reduction or dissolution by acidic fluids. Both scenarios are highly unlikely, as the Fe-depleted regions are confined to distinct layers of

the mound. Silicification clearly aids the preservation of extracellular stalks in Fe-rich horizons. We therefore assume that the silica-rich layers never contained appreciable amounts of Fe and hence that the tubes are unrelated to microbial Fe oxidation. Instead, we propose that the strict parallel alignment of tubes suggests inorganically controlled precipitation. Chemical gardens are well-known for complex inorganic tube structures that are produced by the simple addition of a multivalent metal salt to an alkaline silica solution (e.g., Barge et al., 2012; Cartwright, Garcia-Ruiz, Novella, & Otálora, 2002). Considering the high content of both silica and metal ions in the low-temperature fluids emanating from seafloor hydrothermal systems, these are prospective candidates for natural growth of chemical gardens.

4.2 | Growth and early diagenetic evolution of biomineralized filaments

4.2.1 | Fe mineralization and adsorption

This study is the first to use FIB-TEM to investigate the interiors of silicified extracellular stalks of Fe-oxidizing bacteria and thereby adds another dimension to the biogenicity assessment. STEM-EDS mapping and TEM diffraction analyses (Figure S8) confirm that the stalks in the Jan Mayen mound deposits are composed of an amorphous, siliceous Fe phase. The total lack of crystalline Fe phases contrasts with results obtained from cultures of *Gallionella ferrugina* and *Mariprofundus ferrooxydans* showing elongate akaganeite crystals associated with organic fibrils in stalks cores (Chan et al., 2004; Chan, Fakra, Edwards, Emerson, & Banfield, 2009) and bladed lepidocrocite crystals radiating from the surfaces of freshly grown stalks (Byrne, Schmidt, Gauger, Bryce, & Kappler, 2018; Chan et al., 2011; Comolli et al., 2011). Co-precipitation promotes the formation of immobile linkages between silica and ferrihydrite particles, which retard the transformation of ferrihydrite to crystalline iron oxides (Cornell, Giovanoli, & Schindler, 1987). It is therefore not surprising that the biomineralized stalks in the silica-rich hydrothermal deposits at the JMVF are primarily composed of an amorphous Fe phase.

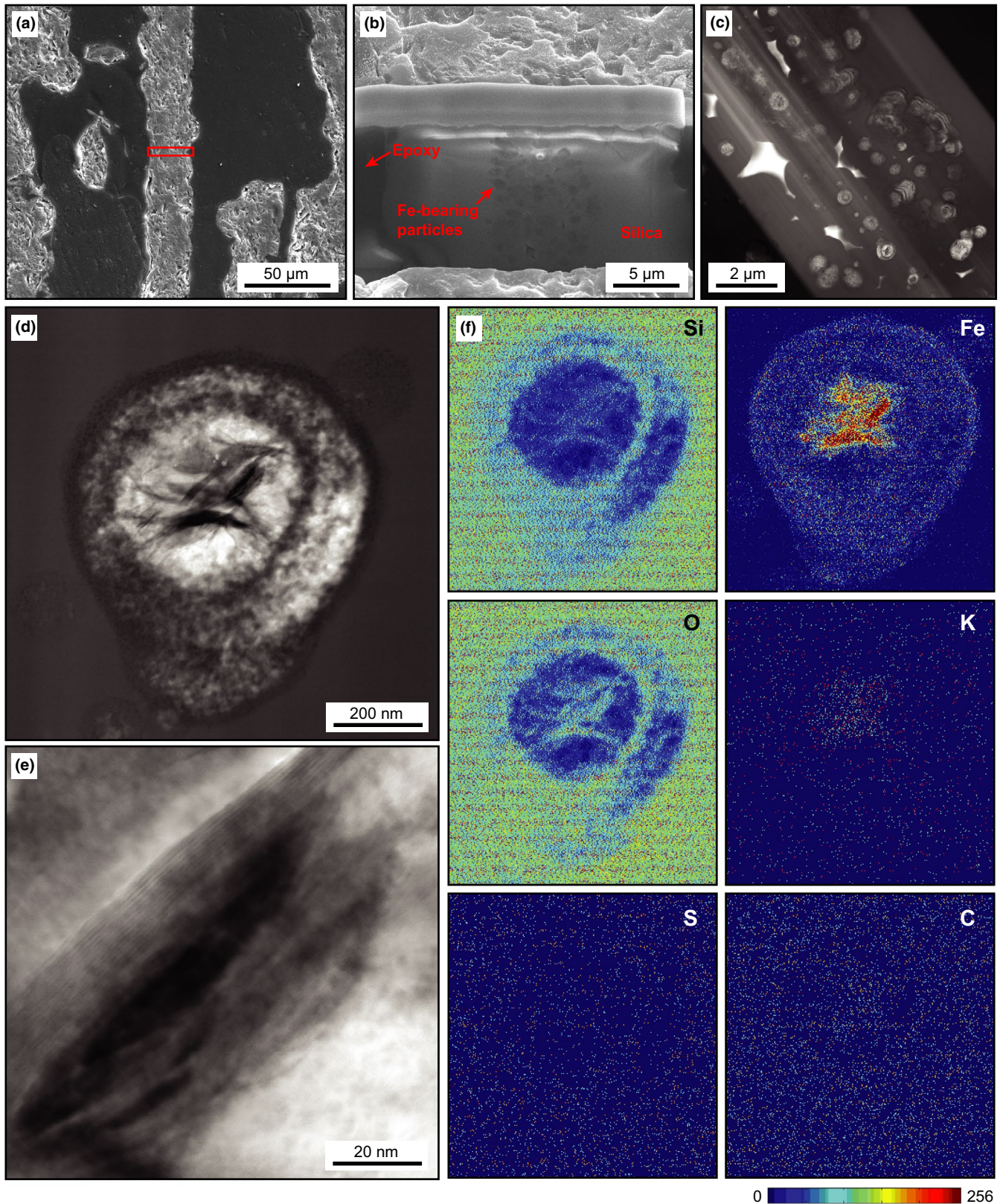
Scanning electron microscopy observations of typical ultrastructural properties of stalk, tube, and sheath interiors (Figure S3) have enabled us to link each of the FIB-TEM cross sections to a distinct filament morphotype. Twisted stalks are easily recognized by their asymmetric cross sections, solid cores, and central porosity (Figure 6;

Figure S3a-d) and represent the most abundant morphology in the FIB-TEM samples (Figure S7). An additional type of cross section is identified by its large, silica-fringed central pores (Figure 7). The jagged inner surface and elliptical outer morphology of the FIB-TEM cross section correspond well with the SEM observations of branching tubes (see Figure S3e, f).

STEM imaging and EDS mapping of the Fe-rich portions of the stalk cross sections reveal distinct core and rim components that differ in terms of grain packing, homogeneity, and chemical composition. The twisted stalks display densely packed, homogeneous cores with elevated concentrations of P along the margins (see Figure 6d,e). Studies of freshwater Fe-oxidizing bacteria have demonstrated that P is evenly distributed in the extracellular Fe-oxyhydroxide stalks (Suzuki et al., 2011). The uneven distribution of P in the stalk cross sections from the JMVF suggests that P adsorption is a more significant process than co-precipitation during stalk growth at this site. Phosphate can be mobilized in low-temperature hydrothermal fluids at depth as a result of Fe-oxyhydroxide dissolution (Johannessen et al., 2017) promoted by microbial dissimilatory iron reduction (Jensen, Mortensen, Andersen, Rasmussen, & Jensen, 1995) or chemical reduction by H_2S under anoxic conditions (Afonso & Stumm, 1992; Kraal, Slomp, Reed, Reichart, & Poulton, 2012). Phosphate groups are efficiently resorbed by fresh Fe-oxyhydroxide particles in the oxic zone near the sediment surface. We postulate that progressive filling of sorption sites on the stalk surface immediately following stalk growth could account for the elevated P content evident around the innermost core region.

Concentric Fe-oxyhydroxide laminae of variable ultrastructure and chemical composition enclose the core region of the twisted stalks. While the core is composed of homogeneous precipitates, the concentric laminae display granular ultrastructure, suggesting disparate formation mechanisms for the internal and external stalk components. The concentric mineralization pattern and local variations in Si and S content between laminae (Figure 6e) indicate that chemically distinct hydrothermal pulses control the precipitation of Fe-oxyhydroxides on the stalk surface following the initial stalk excretion and biomineralization. Stepwise thickening of stalks is consistent with results obtained in laboratory experiments, which show that abiotic oxidation contributes considerably to Fe-oxyhydroxide precipitation on the stalk surface over time (Byrne et al., 2018; Krepski et al., 2013).

FIGURE 8 Filament from the Si-Fe chimney. (a) SEM image of the target filament before FIB milling. The area selected for FIB preparation is marked by red rectangle. (b) SEM image captured during preparation of the FIB-TEM foil. The light gray-dark gray transition seen on the left side of the image is the boundary between the silica and the epoxy used for embedding. (c) Bright field transmission electron microscopy (BF TEM) image of the core of the filament, which is composed of spherical features dispersed in a homogenous, porous matrix. Only the core of the filament (light gray area) has been thinned to <200 nm. (d) BF TEM image of one of the spherical features in the filament core. (e) Close-up image of the center of the spherical feature showing bands with regular d-spacing of 2.2 Å. (f) EDS element maps of the spherical feature. Fe is present throughout, but is strongly enriched in the thin, crystalline bands located in the center. A slight K-enrichment is also evident in these bands. The abundance of Si is lower in the core region than in the surrounding matrix. The intensity scale ranges from 0 to 256



4.2.2 | Degradation of organic carbon template

Stalk-forming Fe-oxidizing bacteria produce polysaccharide templates as a strategy to localize the deposition of Fe-oxyhydroxides and avoid cell encrustation (Chan et al., 2011), and it has been

demonstrated that the organic matrix is retained in extracellular stalks exposed to experimental diagenesis (Picard, Kappler, Schmid, Quaroni, & Obst, 2015). Both SEM and TEM imaging of the JMVF twisted stalks clearly show 10- to 50-nm-wide cavities in the core region (see Figure 6d; Figure S3a,b). EDS mapping (Figure 6e)

indicates neither elevated concentrations of C in association with these cavities nor concentrations above background level in the remaining innermost core, as would be expected if the stalks contain remnants of organic polymers. We cannot exclude that the exceedingly low content of organic C is a primary feature of these stalks (c.f., Bennett, Toner, Barco, & Edwards, 2014), but we find it equally conceivable that the conspicuous cavities in the stalk cores represent empty remains of an organic framework. If the cavities initially accommodated organic templates, the absence of an elevated C EDS signal indicates that templating polysaccharides are easily lost during early diagenesis in natural hydrothermal settings.

One of the studied stalks displays a clearly elevated C signal in the concentrically laminated surface precipitates (Figure 6e). Contamination by epoxy during sample preparation can be excluded as a source of the C enrichment because the EDS maps do not reveal excess Cl in association with the enhanced C signal (see Figure S9 for EDS spectrum of epoxy). C-enriched parts of the sample furthermore display slightly elevated N concentrations (see Figure S8e). The C enrichment may either result from small-scale migration of organic polymers from the stalk core to the periphery during hydrothermal alteration or from the addition of externally sourced organic compounds after stalk formation. Bennett et al. (2014) found that organic carbon derived from cell death and exudation may be remobilized in solution and adsorbed to the surfaces of Fe-oxyhydroxide stalks. The JMVF Fe deposits are exposed to periodic fluxes of hydrothermal fluids, which alter the chemistry of the precipitates and may redistribute organic C from deeper parts of the system. We therefore caution that the presence of C in the vicinity of putative Fe-oxidizing microfossils is not always robust evidence of biogenicity, and that when interpreting microtextures in ancient jaspers, for example, from the 3.77 Gyr Nuvvuagittuq supracrustal belt (Dodd et al., 2017), all possible sources of carbon need to be explored.

4.3 | Biogenicity and growth of filaments and dendrites in the Si-Fe chimney

4.3.1 | Potential biogenic controls on filament growth

A biological origin for the filaments in the chimney fragments is considerably more challenging to discern than for the filaments found in the silicified mounds, as distinct morphological biosignatures of Fe-oxidizing bacteria are absent. Width may serve as a useful tool for determining whether the chimney filaments are stalks of microaerophilic Fe-oxidizing bacteria or abiotic artifacts, because stalk width is constrained by the size of the cell and typically lies within a narrow range (Krepeski et al., 2013). The filamentous structures in the chimney samples are typically between 6 and 12 μm wide and are thus significantly wider than the stalks and sheaths in the laminated mound samples. Additionally, the range of measured widths of chimney filaments is notably larger than that of mound filaments (Figure 5a,b). The diameter of extracellular stalks depends on the extent of surface mineralization and shows substantial variation

between modern samples from different environments and fossil Fe deposits (Hofmann et al., 2008; Krepeski et al., 2013; Little et al., 2004). However, the range of stalk widths within samples from a single locality appears to be relatively narrow. In contrast, abiotic filamentous artifacts may display a large range of widths and a skewed distribution (Hofmann et al., 2008; Rouillard, García-Ruiz, Gong, & Zuilen, 2018). The differences in width distribution in Figure 4 could thus indicate that the filaments in the chimney are of a different origin than the confirmed biogenic stalks in the laminated mounds, although width distributions alone are insufficient to exclude microbial Fe oxidation and stalk mineralization. Internal features and ultrastructure of the chimney filaments provide further evidence that the chimney hosted filaments are unrelated to biomineralized stalks and sheaths. The filament interiors studied by FIB-TEM do not display clear indications of microbial Fe oxidation in the form of distinct Fe-rich cores, but are rather composed of Fe-bearing spherical particles dispersed in silica (Figure 8c). These particles are ca. 0.1–2 μm in diameter and the smallest examples are thus considerably narrower than stalks of Fe-oxidizing bacteria. EDS analyses furthermore show that the Fe is heterogeneously distributed and is largely confined to a cryptocrystalline thread-like phase in the center of some spheres, while the remaining particles contain large amounts of Si (Figure 8e,f).

Multiple branching filaments and dendritic textures are common in the JMVF chimneys (Figure 4) and are key features for determining the biogenicity of the deposits. The multiple branching filaments show branching patterns that are atypical for fabrics generated by stalk- and tube-forming Fe-oxidizing bacteria (e.g., Emerson & Moyer, 2010; Johannessen et al., 2017), exhibiting nodes with more than two branches and growth originating in a single nucleation point (Figure S5c). The lack of distinct sequential bifurcation does not, however, preclude a biogenic origin. Microfossils assigned to the enigmatic genus *Frutexites*, which is known primarily from Fe-rich microbialites, calcareous stromatolites, and subterranean fractures and veins (e.g., Bengtson et al., 2014; Maslov, 1960; Walter & Awramik, 1979), are composed of irregularly formed dendritic iron shrubs. The dendrites in the JMVF chimneys are similar to *Frutexites* with respect to their convex lamination and radially arranged filamentous components. However, *Frutexites* generally displays columnar, stubby branches that may increase in width in the direction of growth (Rodríguez-Martínez, Heim, Quéric, & Reitner, 2011). The dendritic features in the JMVF chimney originate as linear filaments, which show gradually increasing branching frequency in the growth direction. The widths of the branches remain relatively constant and the resulting dendritic textures have a rather slender appearance in comparison to *Frutexites*. Like the associated linear and non-branching filaments, the JMVF dendrites are composed of silica containing variable amounts of dispersed Fe-bearing particles (Figure 4d). Non-branching filaments and dendrites thus appear to be closely related. To our knowledge, *Frutexites* is not commonly found in association with arrays of linear and strongly directional filamentous features. Based on these fundamental geometric discrepancies, the chimney dendrites appear to be unrelated to *Frutexites*.

While stalks were not detected in the chimney samples by SEM, Fe-rich precipitates with globular and vermicular morphology were observed. Aggregates of globular Fe-oxyhydroxides are generally assumed to form by abiotic oxidation (Boyd & Scott, 2001), but the associated nest and tube features display morphological traits that may be linked to microbial activity. The fibrillar, rounded nests found in low abundance in the JMVf chimney (Figure 4g) resemble capsules formed by freshwater Fe oxidizers belonging to the *Siderocapsa* group (Hanert, 2006). Similar nests have also been detected in low-temperature hydrothermal Fe deposits at the Loihi Seamount and ascribed to Fe-oxidizing secondary colonizers (Chan, McAllister, et al., 2016). The short, fibrillar tubes (Figure 4h) may provide shelter for a larger cell, but it is unclear whether the tube walls are generated by passive mineralization of EPS or microbial Fe oxidation. While the rounded nests and fibrillar tubes are likely to be of biogenic origin, there is no apparent link between these features and the silicified filaments and dendrites. The fibrillar features reside on the surfaces of the silica filaments and must postdate filament formation. This observation suggests that nests and fibrillar tubes form late in the growth history of the chimney.

4.3.2 | Potential abiogenic controls on filament growth

Based on filament width distribution, internal distributions of Fe, branching patterns, and morphological characteristics of Fe-rich precipitates, we infer that stalk-forming, Fe-oxidizing bacteria do not play a major role in facilitating Fe mineralization in the hydrothermal Si-Fe chimneys. In the absence of obvious bio-mediated mechanisms for filament growth, purely inorganic processes must be considered. Areas with abundant multiple branching filaments and dendrites commonly display closely spaced bands of decreasing Fe content oriented perpendicularly to the branching direction of the filaments (Figure 4b,c). Some of the bands that are located at the termination of the branching features appear to be completely devoid of Fe. Banded, self-assembled biomorphs have been generated experimentally by autocatalytic co-precipitation of silica and carbonate under locally fluctuating pH conditions (Montalti et al., 2017), and oscillating reaction chemistry is known to produce banded features in natural settings as well (e.g., Liesegang rings; Ortoleva, Chen, & Chen, 1994). Abiotic, non-equilibrium processes have previously been invoked to explain the growth of dendritic iron oxide moss agates produced by oxidizing, silica-rich fluids percolating through hydrothermal sulfide debris (Hopkinson et al., 1998), and manganese dendrites are regarded as products of diffusion-limited reaction processes (e.g., Chopard, Herrmann, & Vicsek, 1991). The lateral variations in the relative contents of Fe and Si in the JMVf chimney dendrites could similarly reflect cyclic variations in micro-environmental conditions. Filament and dendrite growth may be facilitated by cycles of Fe oxidation, Fe-oxyhydroxide supersaturation, nucleation, and temporary depletion controlled by the diffusive transport of Fe(II) to an oxidizing reaction front. We suggest that the

concentration of Fe(II) in the reaction solution at the growth front may exert a primary control on the mode and intensity of filament branching.

4.4 | Effects of environmental parameters on texture development

Textural and paragenetic evidence indicates disparate temperature regimes and formation processes for the JMVf mound and chimney deposits. Based on the observations of twisted stalks, sheaths, and branching tubes, we suggest that the mound deposits originated as microbial mats of Fe-oxidizing bacteria on the seafloor. Considering that the upper temperature limit for growth of *M. ferrooxydans* is ~30°C (Emerson et al., 2007), low-temperature hydrothermal fluids must have sustained initial mound formation. A shift toward higher-temperature, Si-rich fluid discharge would eventually have led to silica mineralization within the pores of Fe-rich horizons and in cavities, thereby encrusting individual filaments and preserving microbial mat textures.

The studied chimney deposit does not display morphological evidence for primary microbial Fe oxidation. Fe-bearing phases are largely present as spherical particles located within silica filaments (Figure 4d). The deposit lacks clearly defined Si- and Fe-rich laminae, but shows distinct small-scale variations in Fe content. We suggest that the gradual exhaustion of Fe with filament and dendrite growth demonstrates coeval Fe-oxyhydroxide and silica precipitation controlled by diffusion and changing availability with progressive mineralization. The large height to width ratio and consistent diameter of the chimney (see Figure 1c) probably result from persistently high concentrations of silica in the hydrothermal fluid, facilitating rapid lithification and upward growth. Considering these geometric and mineralogical characteristics, we infer focused flow and likely higher temperatures than associated with mound growth. O-isotope data from siliceous hydrothermal chimneys at other vent fields indicate silica precipitation at temperatures between ca. 32 and 71°C (Dekov et al., 2015; Herzig, Becker, Stoffers, Bäcker, & Blum, 1988; Stüben et al., 1994; Sun et al., 2012). This range does not overlap with the reported upper temperature limit of 30°C for growth of *M. ferrooxydans* (Emerson et al., 2007).

4.5 | Evaluating filamentous biosignatures in Fe deposits

Morphology is a key property when evaluating putative traces of early life on Earth. The twisted shape of extracellular iron stalks is a prime example of a diagnostic trait that is linked to physiology and may promote the recognition of Fe-oxidizing micro-organisms in the rock record (Chan et al., 2011). It is, however, well-known that abiogenic processes are capable of producing filamentous features that may easily be mistaken for remnants of bacteria or biominerals (e.g., Rouillard et al., 2018). Our comparison of textures from the JMVf mounds and chimney demonstrates that even biosignatures considered quite robust can give rise to substantial ambiguity, as a result

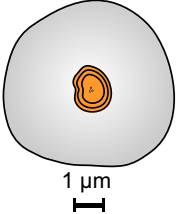
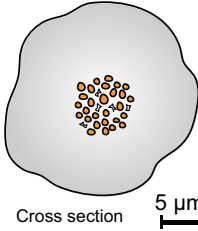
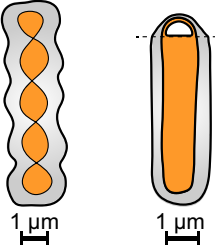
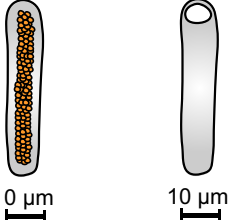
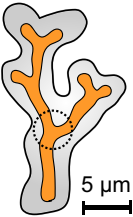
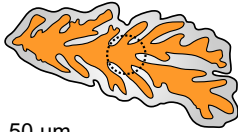
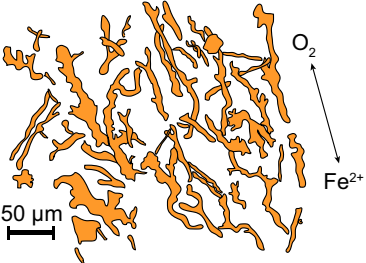
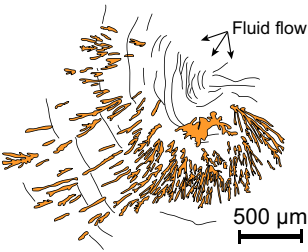
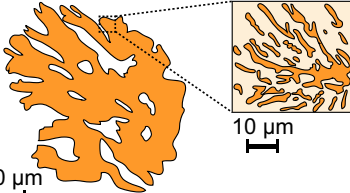
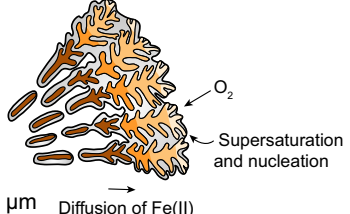
(a) Biosignatures of Fe-oxidizing bacteria		(b) Abiotic filamentous biomorphs	
Feature	Mechanism(s)	Feature	Mechanism(s)
<p>1</p> <p>Solid filament core</p>  <p>1 µm</p>	<p>Encrustation of stalk by silica</p>	<p>1</p> <p>Filament core of separate spherules</p>  <p>Cross section 5 µm</p>	<p>Concurrent precipitation of Fe-bearing phase and silica</p>
<p>2</p> <p>Twisted and tubular morphology</p>  <p>1 µm 1 µm</p>	<p>Metabolic waste disposal</p> <p>Redox stabilization</p> <p>Cell motility</p>	<p>2</p> <p>Wide filaments Hollow silica tubes</p>  <p>10 µm 10 µm</p>	<p>Concurrent precipitation of Fe-bearing phase and silica</p> <p>Chemical garden processes</p>
<p>3</p> <p>Sequential bifurcation</p>  <p>5 µm</p>	<p>Cell division</p>	<p>3</p> <p>Nodes with multiple branches</p>  <p>50 µm</p>	<p>Diffusion limited growth</p>
<p>4</p> <p>Semi-parallel filamentous textures</p>  <p>50 µm</p>	<p>Growth in stable redox gradient</p>	<p>4</p> <p>Highly directional radial textures</p>  <p>500 µm</p>	<p>Fluid flow</p> <p>Rapid diffusion</p>
<p>5</p> <p>Dendritic and radial filamentous textures</p>  <p>200 µm</p>	<p>Growth in a turbulent redox environment</p>	<p>5</p> <p>Banded dendrites</p>  <p>100 µm</p>	<p>Diffusion limited growth</p> <p>Saturation cycles</p>

FIGURE 9 Proposed criteria for the distinction of extracellular filaments of Fe-oxidizing bacteria from abiotic artifacts in the rock record. (a) Ultrastructures and textures that may be associated with stalk- and tube-forming Fe-oxidizing bacteria and proposed developing mechanisms. Biosignatures 2, 3, and 4 and their connection to bacterial physiology have been described previously by, for example, Chan et al. (2011), Comolli et al. (2011), Krepski et al., (2013) and Chan, McAllister, et al. (2016). (b) Ultrastructures and textures that may be associated with abiotically grown filaments and proposed mechanisms of formation

of both post-depositional diagenetic alteration and resemblance to abiogenic features. Figure 9 outlines the processes associated with the growth of extracellular stalks and tubes of microaerophilic Fe-oxidizing bacteria and abiogenic filamentous biomorphs in low-temperature hydrothermal environments and compares the resulting textural and ultrastructural characteristics. The following summary of the main properties of filaments and textures in the studied JMVf samples shed light on the utility of individual biosignatures previously suggested for Fe-oxidizing bacteria.

Organic carbon is a key component of life and the detection of C in microfossils has successfully been applied to support the identification of microbes in ancient environments harboring photosynthetic and heterotrophic organisms (e.g., Wacey et al., 2013; Wacey et al., 2012). Considering the lack of preserved C in the studied stalks from the mildly altered JMVf mounds, organic C does not appear to be a useful biosignature in the search for microaerophilic Fe-oxidizing bacteria in hydrothermally affected deposits, despite its presence in stalks from fresh environmental samples (Chan et al., 2009; Suzuki et al., 2011) and cultures exposed to elevated temperatures (Picard et al., 2015). The paucity of C either reflects a primary lack of organic substances in the stalks (c.f., Bennett et al., 2014) or suggests remobilization of C by hydrothermal fluids, a process that may have affected many of the ancient seafloor habitats for Fe-oxidizing bacteria.

The width distribution of filament assemblages is considered useful for evaluating the biogenicity of iron microfossils because microaerophilic Fe-oxidizing bacteria produce extracellular stalks with fairly uniform widths (Krepski et al., 2013). Individual twisted stalks and sheaths typically display minor changes in width from filament inception to termination, but the thickness may increase toward branching points and decrease abruptly following bifurcation (Chan et al., 2011). Our JMVf work supports that abiogenic filamentous features show a wider range of sizes than biogenic filaments, as noted by Hofmann et al. (2008), and furthermore demonstrates that heterogeneous oxidation and abiogenic Fe-oxyhydroxide and silica mineralization exert a major effect on stalk growth and final widths in hydrothermal systems. Measurements of absolute widths should therefore be considered together with width distributions.

Fe-oxidizing bacteria preferably grow toward zones of higher oxygen concentrations. Consequently, extracellular stalks commonly display directional orientation (Chan, McAllister, et al., 2016; Krepski et al., 2013). The preferred stalk orientation has a clear physiological purpose. Directionality therefore serves as a reasonably strong biosignature for Fe-oxidizing bacteria. While twisted *Mariprofundus*-like stalks generally show clear directionality in Fe deposits in the natural hydrothermal environment at the JMVf (Figure 5c; Figure 9a, 4) filaments may also grow directionally by abiogenic mechanisms.

In fact, abiogenic filamentous textures show exceptionally strong directionality at a small scale (Figure 5d), while the filament orientations shift radially at a larger scale (Figure S5a,b; Figure 9b, 4). These observations demonstrate the need to evaluate mesoscale banding and other larger-scale textures prior to interpreting the origin of directional filaments.

Branching of filaments is another biosignature that is strongly linked to microbial behavior, as it commonly reflects binary cell division (Emerson & Moyer, 2010). However, examples of both putative biogenic and abiogenic branching filaments are present in the JMVf Si-Fe deposits. The extracellular stalks and tubes of microaerophilic Fe-oxidizing bacteria in our samples show relatively simple branching patterns characterized by bifurcation (Figure 9a, 3). Filaments with single branching points are more common than filaments with multiple consecutive nodes. Typical features of abiogenic branching include growth originating in a single particle, nodes that harbor more than two branches, and complex patterns with multiple closely spaced branching points (Figure S5c; Figure 9b, 3). While abiogenic mechanisms have previously been favored to explain dendrites in hydrothermal jasper deposits (Little et al., 2004), our study indicates that Fe-bearing dendrites can grow either by biogenic or abiogenic mechanisms. The microscopy results from the JMVf mound deposit demonstrate that radial associations of twisted stalks produced by Fe-oxidizing bacteria can generate dendritic textures that are not primarily attributed to filament branching (Figure 9a, 5). Consequently, microbial Fe oxidation should be considered a possible driver of dendrite growth in ancient Fe-rich environments. Based on textural evidence from the Si-Fe chimney, we caution that dendrite formation may also be controlled by inorganic processes. The dendritic chemical precipitates are, however, composed of Fe-bearing particles rather than stalks (Figure 9b, 1) and are easily distinguished from the dendritic stalk assemblages by their high silica content, multiple wide branches, and Fe concentration bands, as well as their systematic increase in branching intensity in the growth direction (Figure 4b, c; Figure 9b, 5).

5 | CONCLUSIONS

We have used optical and scanning electron microscopy in combination with focused ion beam-transmission electron microscopy to characterize the differences between biogenic and abiogenic Fe-oxide filament growth in early diagenetic low-temperature Si-Fe deposits from the Jan Mayen Vent Fields. Overall, the results of our study indicate that hydrothermal fluid flow and diffusion-limited reaction processes may produce filamentous features in abiotically controlled systems, albeit with some notable differences with respect to microbial textures.

Abiogenic filamentous features can be distinguished from silicified extracellular stalks of Fe-oxidizing bacteria by their larger diameters, strongly preferred orientation, intense non-bifurcating branching patterns, Fe concentration bands, and particulate interiors. Our study shows that dendrites may originate from local radial growth of stalks of Fe-oxidizing bacteria or by inorganic non-equilibrium reactions, with the latter giving rise to systematically increasing branching intensity in the growth direction. The absence of primary carbon in the silicified Fe deposits at the JMVf demonstrates the high mobility of organic material in hydrothermal environments and casts doubt on whether carbon can be retained in stalks through diagenetic and metamorphic reworking. These findings do not categorically exclude that carbon may be preserved in situ during natural diagenesis of extracellular stalks, but on the basis of our results we would not recommend the detection of organic carbon as a prerequisite for identifying stalk-forming Fe-oxidizing bacteria in the rock record. In this regard, microfossils of Fe-oxidizing stalk formers differ from *bona fide* organic microfossils for which the presence of organic carbon is a necessary requirement.

ACKNOWLEDGMENTS

This study is funded by the University of Bergen and the Research Council of Norway through the Centre for Geobiology (Grant Number 179560), the Foundation Kristian Gerhard Jebsen, and the Bergen Research Foundation (grant awarded to NM). The Research Council of Norway is acknowledged for the support to NTNU NanoLab through the Norwegian Micro- and Nano-Fabrication Facility, NorFab (Grant Number 197411/V30). The TEM work was carried out on NORTEM infrastructure, Grant Number 197405, TEM Gemini Centre, Norwegian University of Science and Technology (NTNU), Norway. NM acknowledges support from the DST-NRF Centre for Excellence in Palaeosciences at the University of Witwatersrand. We thank Irene Heggstad for assistance with SEM and for photographing samples.

ORCID

Karen C. Johannessen  <https://orcid.org/0000-0001-8790-8123>

Nicola McLoughlin  <https://orcid.org/0000-0003-0410-5160>

REFERENCES

- Afonso, M. S., & Stumm, W. (1992). Reductive dissolution of Iron(III) (Hydr)oxides by hydrogen sulfide. *Langmuir*, 8, 1671–1675. <https://doi.org/10.1021/la00042a030>
- Alt, J. C. (1988). Hydrothermal oxide and nontronite deposits on seamounts in the Eastern Pacific. *Marine Geology*, 81, 227–239. [https://doi.org/10.1016/0025-3227\(88\)90029-1](https://doi.org/10.1016/0025-3227(88)90029-1)
- Barge, L. M., Doloboff, I. J., White, L. M., Stucky, G. D., Russell, M. J., & Kanik, I. (2012). Characterization of iron-phosphate-silica chemical garden structures. *Langmuir*, 28, 3714–3721.
- Bekker, A., Slack, J. F., Planavsky, N., Kraepel, B., Hofmann, A., Konhauser, K. O., & Rouxel, O. J. (2010). Iron formation: The sedimentary product of a complex interplay among mantle, tectonic, oceanic, and biospheric processes. *Economic Geology*, 105, 467–508. <https://doi.org/10.2113/gsecongeo.105.3.467>
- Bengtson, S., Ivarsson, M., Astolfo, A., Belivanova, V., Broman, C., Marone, F., & Stampanoni, M. (2014). Deep-biosphere consortium of fungi and prokaryotes in Eocene subseafloor basalts. *Geobiology*, 12, 489–496. <https://doi.org/10.1111/gbi.12100>
- Bennett, S. A., Toner, B. M., Barco, R. A., & Edwards, K. J. (2014). Carbon adsorption onto Fe oxyhydroxide stalks produced by a lithotrophic iron-oxidizing bacteria. *Geobiology*, 12, 146–156.
- Bernis, K., Lowell, R. P., & Farough, A. (2012). Diffuse flow on and around hydrothermal vents at mid-ocean ridges. *Oceanography*, 25, 182–191. <https://doi.org/10.5670/oceanog.2012.16>
- Boyce, A. J., Little, C. T. S., & Russell, M. J. (2003). A new fossil vent biota in the Ballynoe barite deposit, Silvermines, Ireland: Evidence for intracratonic sea-floor hydrothermal activity about 352 Ma. *Economic Geology*, 98, 649–656. <https://doi.org/10.2113/98.3.649>
- Boyd, T. D., & Scott, S. D. (2001). Microbial and hydrothermal aspects of ferric oxyhydroxides and ferrous hydroxides: the example of Franklin Seamount, Western Woddlark Basin, Papua New Guinea. *Geochemical Transactions*, 2, 7.
- Breier, J. A., Gomez-Ibanez, D., Reddington, E., Huber, J. A., & Emerson, D. (2012). A precision multi-sampler for deep-sea hydrothermal microbial mat studies. *Deep-Sea Research I*, 70, 83–90. <https://doi.org/10.1016/j.dsr.2012.10.006>
- Byrne, J. M., Schmidt, M., Gauger, T., Bryce, C., & Kappler, A. (2018). Imaging organic-mineral aggregates formed by Fe(II)-oxidizing bacteria using helium ion microscopy. *Environmental Science and Technology Letters*, 5, 209–213. <https://doi.org/10.1021/acs.estlett.8b00077>
- Cartwright, J. H. E., García-Ruiz, J. M., Novella, M. L., & Otálora, F. (2002). Formation of chemical gardens. *Journal of Colloid and Interface Science*, 256, 351–359. <https://doi.org/10.1006/jcis.2002.8620>
- Chan, C. S., De Stasio, G., Welch, S. A., Girasole, M., Frazer, B. H., Nesterova, M. V., ... Banfield, J. F. (2004). Microbial polysaccharides template assembly of nanocrystal fibers. *Science*, 303. <https://doi.org/10.1126/science.1092098>
- Chan, C. S., Emerson, D., & Luther, G. W. (2016). The role of microaerophilic Fe-oxidizing micro-organisms in producing banded iron formations. *Geobiology*, 14(5), 509–528. <https://doi.org/10.1111/gbi.12192>
- Chan, C. S., Fakra, S. C., Edwards, D. C., Emerson, D., & Banfield, J. F. (2009). Iron oxyhydroxide mineralization on microbial extracellular polysaccharides. *Geochimica Et Cosmochimica Acta*, 73, 3807–3818. <https://doi.org/10.1016/j.gca.2009.02.036>
- Chan, C. S., Fakra, S. C., Emerson, D., Fleming, E. J., & Edwards, K. J. (2011). Lithotrophic iron-oxidising bacteria produce organic stalks to control mineral growth: Implications for biosignature formation. *The International Society for Microbial Ecology Journal*, 5, 717–727.
- Chan, C. S., McAllister, S. M., Leavitt, A. H., Glazer, B. T., Krepski, S. T., & Emerson, D. (2016). The architecture of iron microbial mats reflects the adaptation of chemolithotrophic iron oxidation in freshwater and marine environments. *Frontiers in Microbiology*, 7, 1–18. <https://doi.org/10.3389/fmicb.2016.00796>
- Chi Fru, E., Ivarsson, M., Kilias, S. P., Bengtson, S., Belivanova, V., ... Stampanoni, M. (2013). Fossilized iron bacteria reveal a pathway to the biological origin of banded iron formation. *Nature Communications*, 4(1), 1–7. <https://doi.org/10.1038/ncomms3050>
- Chiu, B. K., Kato, S., McAllister, S. M., Field, E. K., & Chan, C. S. (2017). Novel pelagic iron-oxidizing zetaproteobacteria from the Chesapeake Bay oxic-anoxic transition zone. *Frontiers in Microbiology*, 8, 1–16. <https://doi.org/10.3389/fmicb.2017.01280>
- Chopard, B., Herrmann, H. J., & Vicsek, T. (1991). Structure and growth mechanism of mineral dendrites. *Nature*, 353, 409–412. <https://doi.org/10.1038/353409a0>
- Comolli, L. R., Luef, B., & Chan, C. S. (2011). High-resolution 2D and 3D cryo-TEM reveals structural adaptations of two stalk-forming bacteria to an Fe-oxidizing lifestyle. *Environmental Microbiology*, 13, 2915–2929.

- Cornell, R. M., Giovanoli, R., & Schindler, P. W. (1987). Effect of silicate species on the transformation of ferrihydrite into goethite and hematite in alkaline media. *Clays and Clay Minerals*, *35*, 21–28. <https://doi.org/10.1346/CCMN.1987.0350103>
- Crosby, C. H., Bailey, J. V., & Sharma, M. (2014). Fossil evidence of iron-oxidizing chemolithotrophy linked to phosphogenesis in the wake of the Great Oxidation Event. *Geology*, *42*, 1015–1018. <https://doi.org/10.1130/G35922.1>
- Dekov, V. M., Lalonde, S. V., Kamenov, G. D., Bayon, G., Shanks Iii, W. C., Fortin, D., ... Moscati, R. J. (2015). Geochemistry and mineralogy of a silica chimney from an inactive seafloor hydrothermal field (East Pacific Rise, 18°S). *Chemical Geology*, *415*, 126–140. <https://doi.org/10.1016/j.chemgeo.2015.09.017>
- Dodd, M. S., Papineau, D., Grenne, T., Slack, J. F., Rittner, M., Pirajno, F., ... Little, C. T. S. (2017). Evidence for early life in Earth's oldest hydrothermal vent precipitates. *Nature*, *543*, 60–64. <https://doi.org/10.1038/nature21377>
- Duhig, N. C., Davidson, G. J., & Stolz, J. (1992). Microbial involvement in the formation of Cambrian sea-floor silica-iron oxide deposits, Australia. *Geology*, *20*, 511–514. [https://doi.org/10.1130/0091-7613\(1992\)020<0511:MIITFO>2.3.CO;2](https://doi.org/10.1130/0091-7613(1992)020<0511:MIITFO>2.3.CO;2)
- Edwards, K. J., Glazer, B. T., Rouxel, O. J., Bach, W., Emerson, D., Davis, R. E., ... Moyer, C. L. (2011). Ultra-diffuse hydrothermal venting supports Fe-oxidizing bacteria and massive amber deposition at 5000 m off Hawaii. *The International Society for Microbial Ecology Journal*, *5*, 1748–1758.
- Edwards, K. J., Rogers, D. R., Wirsén, C. O., & McCollom, T. M. (2003). Isolation and characterization of novel psychrophilic, neutrophilic, Fe-Oxidizing, chemolithoautotrophic α - and γ -*Proteobacteria* from the deep sea. *Applied and Environmental Microbiology*, *69*, 2906–2913.
- Emerson, D., & Moyer, C. L. (2002). Neutrophilic Fe-Oxidizing bacteria are abundant at the Loihi seamount hydrothermal vents and play a major role in Fe oxide deposition. *Applied and Environmental Microbiology*, *68*, 3085–3093. <https://doi.org/10.1128/AEM.68.6.3085-3093.2002>
- Emerson, D., & Moyer, C. L. (2010). Microbiology of seamounts. Common patterns observed in community structure. *Oceanography*, *23*, 148–163. <https://doi.org/10.5670/oceanog.2010.67>
- Emerson, D., & Revsbech, N. P. (1994). Investigation of an iron-oxidizing microbial mat community located near Aarhus, Denmark: Field studies. *Applied and Environmental Microbiology*, *60*, 4022–4031.
- Emerson, D., Rentz, J. A., Lilburn, T. G., Davis, R. E., Aldrich, H., Chan, C., & Moyer, C. L. (2007). A novel lineage of proteobacteria involved in formation of marine Fe-oxidizing microbial mat communities. *PLoS one*, *2*(8), e667.
- Emerson, D., Scott, J. J., Leavitt, A., Fleming, E., & Moyer, C. (2017). In situ estimates of iron-oxidation and accretion rates for iron-oxidizing bacterial mats at Lō'ihi Seamount. *Deep-Sea Research Part I*, *126*, 31–39. <https://doi.org/10.1016/j.dsr.2017.05.011>
- Fleming, E. J., Cetinic, I., Chan, C. S., King, D. W., & Emerson, D. (2014). Ecological succession among iron-oxidizing bacteria. *The International Society for Microbial Ecology Journal*, *8*, 804–815. <https://doi.org/10.1038/ismej.2013.197>
- Fleming, E. J., Davis, R. E., Mcallister, S. M., Chan, C. S., Moyer, C. L., Tebo, B. M., & Emerson, D. (2013). Hidden in plain sight: Discovery of a sheath-forming iron-oxidizing *Zetaproteobacteria* at Loihi Seamount, Hawaii, USA. *FEMS Microbiology Ecology*, *85*, 116–127.
- Forget, N. L., Murdock, S. A., & Juniper, S. K. (2010). Bacterial diversity in Fe-rich hydrothermal sediments at two South Tonga Arc submarine volcanoes. *Geobiology*, *8*, 417–432. <https://doi.org/10.1111/j.1472-4669.2010.00247.x>
- García-Ruiz, J. M., Nakouzi, E., Kotopoulou, E., Tamborrino, L., & Steinbock, O. (2017). Biomimetic mineral self-organization from silica-rich spring waters. *Science Advances*, *3*, e1602285. <https://doi.org/10.1126/sciadv.1602285>
- Ghiorse, W. C. (1984). Biology of iron- and manganese-depositing bacteria. *Annual Review of Microbiology*, *38*, 515–550. <https://doi.org/10.1146/annurev.mi.38.100184.002503>
- Grenne, T., & Slack, J. F. (2003). Bedded jaspers of the Ordovician Løkken ophiolite, Norway: Seafloor deposition and diagenetic maturation of hydrothermal plume-derived silica-iron gels. *Mineralium Deposita*, *38*, 625–639. <https://doi.org/10.1007/s00126-003-0346-3>
- Hanert, H. H. (2006). The Genus *Siderocapsa* (and other Iron- and Manganese-Oxidizing Eubacteria). In M. Dworkin, S. Falkow, E. Rosenberg, K.-H. Schleifer, & E. Stackebrandt (Eds.), *The prokaryotes* (pp. 1005–1015). New York, NY: Springer.
- Heim, C., Quéric, N.-V., Ionescu, D., Schäfer, N., & Reitner, J. (2017). Frutexites-like structures formed by iron oxidizing biofilms in the continental subsurface (Åspö Hard Rock Laboratory, Sweden). *PLoS ONE*, *12*, e0177542. <https://doi.org/10.1371/journal.pone.0177542>
- Herzig, P. M., Becker, K. P., Stoffers, P., Bäcker, H., & Blum, N. (1988). Hydrothermal silica chimney fields in the Galapagos Spreading Center at 86°W. *Earth and Planetary Science Letters*, *89*, 261–272. [https://doi.org/10.1016/0012-821X\(88\)90115-X](https://doi.org/10.1016/0012-821X(88)90115-X)
- Hofmann, B. A., Farmer, J. D., Von Blanckenburg, F., & Fallick, A. E. (2008). Subsurface filamentous fabrics: An evaluation of origins based on morphological and geochemical criteria, with implications for exo-paleontology. *Astrobiology*, *8*, 87–117. <https://doi.org/10.1089/ast.2007.0130>
- Holm, N. G. (1987). Biogenic influences on the geochemistry of certain ferruginous sediments of hydrothermal origin. *Chemical Geology*, *63*, 45–57. [https://doi.org/10.1016/0009-2541\(87\)90073-8](https://doi.org/10.1016/0009-2541(87)90073-8)
- Hopkinson, L., Roberts, S., Herrington, R., & Wilkinson, J. (1998). Self-organization of submarine hydrothermal siliceous deposits: Evidence from the TAG hydrothermal mound, 26°N Mid-Atlantic Ridge. *Geology*, *26*, 347–350. [https://doi.org/10.1130/0091-7613\(1998\)026<0347:SOOSHS>2.3.CO;2](https://doi.org/10.1130/0091-7613(1998)026<0347:SOOSHS>2.3.CO;2)
- Jensen, H. S., Mortensen, P. B., Andersen, F. Ø., Rasmussen, E., & Jensen, A. (1995). Phosphorus cycling in a coastal marine sediment, Aarhus Bay, Denmark. *Limnology and Oceanography*, *40*, 908–917. <https://doi.org/10.4319/lo.1995.40.5.0908>
- Johannessen, K. C., Vander Roost, J., Dahle, H., Dundas, S. H., Pedersen, R. B., & Thorseth, I. H. (2017). Environmental controls on biomineralization and Fe-mound formation in a low-temperature hydrothermal system at the Jan Mayen Vent Fields. *Geochimica Et Cosmochimica Acta*, *202*, 101–123. <https://doi.org/10.1016/j.gca.2016.12.016>
- Juniper, S. K., & Fouquet, Y. (1988). Filamentous iron-silica deposits from modern and ancient hydrothermal sites. *Canadian Mineralogist*, *26*, 859–869.
- Kappler, A., Pasquero, C., Konhauser, K. O., & Newman, D. K. (2005). Deposition of banded iron formations by anoxygenic phototrophic Fe(II)-oxidizing bacteria. *Geology*, *33*, 865–868. <https://doi.org/10.1130/G21658.1>
- Karl, D. M., Brittain, A. M., & Tilbrook, B. D. (1989). Hydrothermal and microbial processes at Loihi Seamount, a mid-plate hot-spot volcano. *Deep-Sea Research*, *36*, 1655–1673. [https://doi.org/10.1016/0198-0149\(89\)90065-4](https://doi.org/10.1016/0198-0149(89)90065-4)
- Kato, S., Kobayashi, C., Kakegawa, T., & Yamagishi, A. (2009). Microbial communities in iron-silica-rich microbial mats at deep-sea hydrothermal fields of the Southern Mariana Through. *Environmental Microbiology*, *11*, 2094–2111.
- Kennedy, C. B., Scott, S. D., & Ferris, F. G. (2003). Characterization of bacteriogenic iron oxide deposits from Axial Volcano, Juan de Fuca Ridge, Northeast Pacific Ocean. *Geomicrobiology Journal*, *20*, 199–214. <https://doi.org/10.1080/01490450303873>
- Klein, C. (2005). Some Precambrian banded iron-formations (BIFs) from around the world: Their age, geologic setting, mineralogy, metamorphism, geochemistry, and origin. *American Mineralogist*, *90*, 1473–1499.

- Konhäuser, K. O., Hamade, T., Raiswell, R., Morris, R. C., Ferris, F. G., Southam, G., & Canfield, D. E. (2002). Could bacteria have formed the Precambrian banded iron formations? *Geology*, *30*, 1079–1082. [https://doi.org/10.1130/0091-7613\(2002\)030<1079:CBHFTP>2.0.CO;2](https://doi.org/10.1130/0091-7613(2002)030<1079:CBHFTP>2.0.CO;2)
- Kraal, P., Slomp, C. P., Reed, D. C., Reichart, G.-J., & Poulton, S. W. (2012). Sedimentary phosphorus and iron cycling in and below the oxygen minimum zone of the northern Arabian Sea. *Biogeosciences*, *9*, 2603–2624. <https://doi.org/10.5194/bg-9-2603-2012>
- Krepeski, S. T., Emerson, D., Hredzak-Showalter, P. L., Luther, G. W., & Chan, C. S. (2013). Morphology of biogenic iron oxides records microbial physiology and environmental conditions: Toward interpreting iron microfossils. *Geobiology*, *11*, 457–471. <https://doi.org/10.1111/gbi.12043>
- Langley, S., Igric, P., Takahashi, Y., Sakai, Y., Fortin, D., Hannington, M. D., & Schwarz-Schampera, U. (2009). Preliminary characterization and biological reduction of putative biogenic iron oxides (BIOS) from the Tonga-Kermadec Arc, southwest Pacific Ocean. *Geobiology*, *7*, 35–49. <https://doi.org/10.1111/j.1472-4669.2008.00180.x>
- Li, J., Zhou, H., Peng, X., Wu, Z., Chen, S., & Fang, J. (2012). Microbial diversity and biomineralization in low-temperature hydrothermal iron-silica-rich precipitates of the Lau Basin hydrothermal field. *FEMS Microbiology Ecology*, *81*, 205–216. <https://doi.org/10.1111/j.1574-6941.2012.01367.x>
- Little, C. T. S., Glynn, S. E., & Mills, R. A. (2004). Four-hundred-and-ninety-million-year record of bacteriogenic iron oxide precipitation at sea-floor hydrothermal vents. *Geomicrobiology Journal*, *21*, 415–429. <https://doi.org/10.1080/01490450490485845>
- Little, C. T. S., & Thorseth, I. H. (2002). Hydrothermal vent microbial communities: A fossil perspective. *Cahiers De Biologie Marine*, *43*, 317–319.
- Lyons, T. W., Reinhard, C. T., & Planavsky, N. J. (2014). The rise of oxygen in Earth's early ocean and atmosphere. *Nature*, *506*, 307–315. <https://doi.org/10.1038/nature13068>
- Maslov, V. P. (1960). *Stromatolites*. Moscow, Russia: Trudy Instituta geologicheskikh nauk Akademiya nauk SSR.
- McAllister, S. M., Moore, R. M., Gartman, A., Luther, G. W. III, Emerson, D., & Chan, C. S. (2019). The Fe(II)-oxidizing Zetaproteobacteria: Historical, ecological and genomic perspectives. *FEMS Microbiology Ecology*, *95*, 1–18.
- Melton, E. D., Swanner, E. D., Behrens, S., Schmidt, C., & Kappler, A. (2014). The interplay of microbially mediated and abiotic reactions in the biogeochemical Fe cycle. *Nature Reviews Microbiology*, *12*, 797–808. <https://doi.org/10.1038/nrmicro3347>
- Moeller, K., Schoenberg, R., Grenne, T., Thorseth, I. H., Drost, K., & Pedersen, R. B. (2014). Comparison of iron isotope variations in modern and Ordovician siliceous Fe oxyhydroxide deposits. *Geochimica Et Cosmochimica Acta*, *126*, 422–440. <https://doi.org/10.1016/j.gca.2013.11.018>
- Montalti, M., Zhang, G., Genovese, D., Morales, J., Kellermeier, M., & García-Ruiz, J. M. (2017). Local pH oscillations witness autocatalytic self-organization of biomorphic nanostructures. *Nature Communications*, *8*, 14427. <https://doi.org/10.1038/ncomms14427>
- Ortoleva, P., Chen, Y., & Chen, W. (1994). Agates, geodes, concretions and orbicules: Self-organized zoning and morphology. In J. H. Kruhl (Ed.), *Fractals and dynamic systems in geoscience*. Heidelberg, Germany: Springer, Berlin.
- Park, S. S., Lee, C. H., Cheon, J. H., & Park, D. H. (2001). Formation mechanism of PMO with rope- and gyroid-based morphologies via close packing of secondary building units. *Journal of Materials Chemistry*, *11*, 3397–3403.
- Pedersen, R. B., Thorseth, I. H., Nygård, T. E., Lilley, M. D., & Kelley, D. S. (2010). Hydrothermal activity at the Arctic Mid-Ocean Ridges. In P. A. Rona, C. W. Devey, J. Dymont, & B. J. Murton (Eds.), *Diversity of hydrothermal systems on slow spreading Ocean Ridges* (pp. 67–89). Washington, DC: Geophysical Monograph Series.
- Peng, X., Ta, K., Chen, S., Zhang, L., & Xu, H. (2015). Coexistence of Fe(II)- and Mn(II)-oxidizing bacteria govern the formation of deep sea amber deposits. *Geochimica Et Cosmochimica Acta*, *169*, 200–216. <https://doi.org/10.1016/j.gca.2015.09.011>
- Picard, A., Kappler, A., Schmid, G., Quaroni, L., & Obst, M. (2015). Experimental diagenesis of organo-mineral structures formed by microaerophilic Fe (II)-oxidizing bacteria. *Nature Communications*, *6*.
- Planavsky, N., Rouxel, O., Bekker, A., Shapiro, R., Fralick, P., & Knudsen, A. (2009). Iron-oxidizing microbial ecosystems thrived in late Paleoproterozoic redox-stratified oceans. *Earth and Planetary Science Letters*, *286*, 230–242. <https://doi.org/10.1016/j.epsl.2009.06.033>
- Rodríguez-Martínez, M., Heim, C., Quéric, N.-V., & Reitner, J. (2011). Frutexites. In J. Reitner, & V. Thiel (Eds.), *Encyclopedia of geobiology* (pp. 396–401). Dordrecht, Netherlands: Springer.
- Rouillard, J., García-Ruiz, J.-M., Gong, J., & van Zuilen, M. A. (2018). A morphogram for silica-witherite biomorphs and its application to microfossil identification in the early earth rock record. *Geobiology*, *16*, 279–296. <https://doi.org/10.1111/gbi.12278>
- Scott, J. J., Breier, J. A., Luther, G. W. III, & Emerson, D. (2015). Microbial iron mats at the mid-atlantic ridge and evidence that zetaproteobacteria may be restricted to iron-oxidizing marine systems. *PLoS ONE*, *10*, e0119284. <https://doi.org/10.1371/journal.pone.0119284>
- Slack, J. F., Grenne, T., & Bekker, A. (2009). Seafloor-hydrothermal Si-Fe-Mn exhalites in the Pecos greenstone belt, New Mexico, and the redox state of ca. 1720 Ma deep seawater. *Geosphere*, *5*, 302–314. <https://doi.org/10.1130/GES00220.1>
- Slack, J. F., Grenne, T., Bekker, A., Rouxel, O. J., & Lindberg, P. A. (2007). Suboxic deep seawater in the late Paleoproterozoic: Evidence from hematitic chert and iron formation related to seafloor-hydrothermal sulfide deposits, central Arizona, USA. *Earth and Planetary Science Letters*, *255*, 243–256. <https://doi.org/10.1016/j.epsl.2006.12.018>
- Sokolev, I., & Kievsky, Y. (2005). 3D Design of self-assembled nanoporous colloids. *Studies in Surface Science and Catalysis*, *156*, 433–442.
- Stüben, D., Taibi, N. E., McMurtry, G. M., Scholten, J., Stoffers, P., & Zhang, D. (1994). Growth history of a hydrothermal silica chimney from the Mariana backarc spreading center (southwest Pacific, 18° 13'N). *Chemical Geology*, *113*, 273–296. [https://doi.org/10.1016/0009-2541\(94\)90071-X](https://doi.org/10.1016/0009-2541(94)90071-X)
- Sun, Z., Li, J., Huang, W., Dong, H., Little, C. T. S., & Li, J. (2015). Generation of hydrothermal Fe-Si oxyhydroxide deposit on the Southwest Indian Ridge and its implication for the origin of ancient banded iron formations. *Journal of Geophysical Research: Biogeosciences*, *120*, 187–203. <https://doi.org/10.1002/2014JG002764>
- Sun, Z. L., Zhou, H. Y., Yang, Q. H., Yin, Z. J., Wang, H., Yao, H. Q., & Dong, C. F. (2012). Growth model of a hydrothermal low-temperature Si-rich chimney: Example from the CDE hydrothermal field, Lau Basin. *Science China Earth Sciences*, *55*, 1716–1730. <https://doi.org/10.1007/s11430-012-4485-1>
- Suzuki, T., Hashimoto, H., Matsumoto, N., Furutani, M., Kunoh, H., & Takada, J. (2011). Nanometer-scale visualization and structural analysis of the inorganic/organic hybrid structure of *Gallionella ferruginea* twisted stalks. *Applied and Environmental Microbiology*, *77*, 2877–2881. <https://doi.org/10.1128/AEM.02867-10>
- Vander Roost, J., Thorseth, I. H., & Dahle, H. (2017). Microbial analysis of Zetaproteobacteria and co-colonizers of iron mats in the Troll Wall Vent Field. *Arctic Mid-Ocean Ridge. Plos ONE*, *12*, e0185008. <https://doi.org/10.1371/journal.pone.0185008>
- Wacey, D., Mcloughlin, N., Kilburn, M. R., Saunders, M., Cliff, J. B., Kong, C., ... Brasier, M. D. (2013). Nanoscale analysis of pyritized microfossils reveals differential heterotrophic consumption in the ~1.9-Ga Gunflint chert. *PNAS*, *110*, 8020–8024.

- Wacey, D., Menon, S., Green, L., Gerstmann, G., Kong, C., McLoughlin, N., ... Brasier, M. (2012). Taphonomy of very ancient microfossils from the ~3400 Ma Strelley Pool Formation and ~1900 Ma Gunflint Formation: New insights using a focused ion beam. *Precambrian Research*, 220–221, 234–250. <https://doi.org/10.1016/j.precamres.2012.08.005>
- Walter, M. R., & Awramik, S. M. (1979). Frutexites from stromatolites of the Gunflint iron formation of Canada, and its biological affinities. *Precambrian Research*, 9, 23–33. [https://doi.org/10.1016/0301-9268\(79\)90049-4](https://doi.org/10.1016/0301-9268(79)90049-4)

How to cite this article: Johannessen KC, McLoughlin N, Vullum PE, Thorseth IH. On the biogenicity of Fe-oxyhydroxide filaments in silicified low-temperature hydrothermal deposits: Implications for the identification of Fe-oxidizing bacteria in the rock record. *Geobiology*. 2020;18:31–53. <https://doi.org/10.1111/gbi.12363>

SUPPORTING INFORMATION

Additional supporting information may be found online in the Supporting Information section at the end of the article.